Available online at www.sciencedirect.com

ScienceDirect

Geochimica et Cosmochimica Acta 300 (2021) 164–191

Geochimica et Cosmochimica Acta

www.elsevier.com/locate/gca

The uranium isotopic record of shales and carbonates through geologic time

X. Chen [a,*], F.L.H. Tissot [a,b], M.F. Jansen [c], A. Bekker [d,e], C.X. Liu [a], N.X. Nie [f], G.P. Halverson [g], J. Veizer [h], N. Dauphas [a]

[a] *Origins Laboratory, Department of the Geophysical Sciences and Enrico Fermi Institute, The University of Chicago, Chicago, IL, USA*
[b] *The Isotoparium, Division of Geological and Planetary Sciences, Caltech, Pasadena, CA, USA*
[c] *Department of the Geophysical Sciences, The University of Chicago, Chicago, IL, USA*
[d] *Department of Earth and Planetary Sciences, University of California Riverside, Riverside, CA, USA*
[e] *Department of Geology, University of Johannesburg, Johannesburg 2006, South Africa*
[f] *Carnegie Institution for Science, Washington, DC 20005, USA*
[g] *Department of Earth and Planetary Sciences, McGill University, Montreal, Quebec, Canada*
[h] *Department of Earth and Environmental Sciences, University of Ottawa, Ottawa, Canada*

Received 17 October 2019; accepted in revised form 25 January 2021; available online 3 February 2021

Abstract

In the modern ocean, U reduction and incorporation into anoxic sediments imparts a large isotopic fractionation of approximately +0.6‰ that shifts the seawater $\delta^{238}U$ value ($^{238}U/^{235}U$, expressed as $\delta^{238}U$ per mil deviation relative to CRM-112a) relative to continental runoff. Given the long residence time of U in the modern oceans (~400 kyr), the isotopic composition of carbonates (taken as a proxy for seawater) reflects the global balance between anoxic and other sinks. The U isotopic composition of open-marine carbonates has thus emerged as a proxy for reconstructing past changes in the redox state of the global ocean. A tenet of this approach is that the $\delta^{238}U$ values of seawater and anoxic sediments should always be fractionated by the same amount.

In order to test this hypothesis, we have measured the U concentrations and isotopic compositions of carbonates spanning ages from 3250 Ma to present. A first-order expectation for the Archean and possibly Proterozoic is that near-quantitative U removal to extensive anoxic sediments should have shifted the uranium isotopic composition of seawater and carbonates towards lower values. Instead, the measurements reveal that many Archean and Proterozoic carbonates have unfractionated $\delta^{238}U$ values similar to those of continents and riverine runoff. These results are inconsistent with the view that the U isotopic composition of seawater simply reflects the areal extent of anoxic sediments in the past.

We consider two plausible explanations for why the U isotopic composition of Archean and Proterozoic carbonates is not fractionated from the crustal and riverine composition: (1) the residence time of U could have been much shorter in the Precambrian oceans when anoxic settings were much more extensive, and (2) the process of incorporation of U into anoxic sediments in the Precambrian imparted a smaller U isotopic fractionation than in the modern because of differences in the efficiency or mechanism of uranium removal. This study highlights the challenges inherent to applying knowledge of the modern marine U isotopic cycle to periods of Earth's history when ocean-floor anoxia was much more extended, anoxic basins were ferruginous, and atmospheric oxygen content was significantly lower than present.

Keywords: Uranium; Isotopes; Carbonate; Shale; Residence time; Ocean mixing time

* Corresponding author.
E-mail address: chenxicindy@uchicago.edu (X. Chen).

https://doi.org/10.1016/j.gca.2021.01.040
0016-7037/

1. INTRODUCTION

Compared to the relatively well-understood oxygenation history of Earth's atmosphere, the timing and magnitude of oceanic oxygenation is still a matter of debate (*e.g.*, Lyons et al., 2014). Indeed, our understanding of the temporal dynamics and cause-and-effect relationships during critical redox transitions remains limited. Diverse proxies have been developed to address these questions, including the presence or absence of redox-sensitive detrital minerals such as pyrite, uraninite, and siderite in terrestrial and coastal sandstones and conglomerates (Ramdohr, 1958; Rasmussen and Buick, 1999), variations in the elemental abundance of redox-sensitive elements in organic-rich shales (*e.g.*, Co, Cr, I, Mo, Re, U, V, and Zn; Anbar et al., 2007; Scott et al., 2008; Sahoo et al., 2012; Partin et al., 2013a; Reinhard et al., 2013; Hardisty et al., 2014; Scott et al., 2014; Swanner et al., 2014; Hardisty et al., 2017), variations in the isotopic composition of traditional stable isotopes in sedimentary rocks (*e.g.*, S, C, and N; Holland, 2006; Farquhar et al., 2011; Farquhar et al., 2014), and more recently, variations in the non-traditional stable isotopic compositions (*e.g.*, Fe, Mo, Cr, Se, and U; see the review chapters in Teng et al., 2017) of marine sediments (*e.g.*, shales, iron formations, sedimentary pyrites, and carbonates).

The ratio of the two long-lived isotopes of U ($^{238}U/^{235}U$; expressed as $\delta^{238}U$, which is the per mil $^{238}U/^{235}U$ deviation of a sample relative to the CRM-112a standard) has been extensively used to track the global extent of oceanic anoxia through time (Stirling et al., 2007; Weyer et al., 2008; Montoya-Pino et al., 2010; Brennecka et al., 2011; Asael et al., 2013; Kendall et al., 2013, 2015, 2020; Andersen et al., 2014, 2016, 2018; Dahl et al., 2014, 2017, 2019; Azmy et al., 2015; Tissot and Dauphas, 2015; Hood et al., 2016; Lau et al., 2016, 2017; Wang et al., 2016, 2018, 2020; Elrick et al., 2017; Jost et al., 2017; Lu et al., 2017; Song et al., 2017; Yang et al., 2017; Bartlett et al., 2018; Bura-Nakić et al., 2018, 2020; Chen et al., et al., 2018a, 2018b; Clarkson et al., 2018; Herrmann et al., 2018; Phan et al., 2018; Wei et al., 2018, 2020; White et al., 2018; Zhang et al., 2018a, 2018b, 2018c, 2019a, 2019b, 2020a, 2020b, 2020c; Gilleaudeau et al., 2019; Tostevin et al., 2019; Abshire et al., 2020; Brüske et al., 2020a, 2020b; Cao et al., 2020; Cheng et al., 2020; Li et al., 2020; Mänd et al., 2020; del Rey et al., 2020; Stockey et al., 2020; Zhao et al., 2020; Cole et al., 2020) (an up-to-date compilation of $\delta^{238}U$ values of carbonates, shales and iron-rich rocks is provided as a supplementary online Excel spreadsheet). Indeed, uranium is a redox-sensitive element, and its isotopic composition in modern seawater ($\delta^{238}U_{sw}$) reflects the mass balance between riverine input of U (assumed to be the major source) and removal into several sinks (Tissot and Dauphas, 2015; Andersen et al., 2016). In the modern ocean, U occurs in two main oxidation states: highly soluble U(VI), which exists as uranyl carbonate complexes (Langmuir, 1978; Dong and Brooks, 2006; Endrizzi and Rao, 2014; Maloubier et al., 2015), and insoluble U(IV).

The sinks of U in the modern ocean are Fe-Mn nodules, suboxic sediments, oceanic crust alteration, carbonates, deep-sea and anoxic sediments (Dunk et al., 2002). In anoxic settings, U(VI) is reduced to U(IV), which has low solubility and precipitates, presumably through adsorption onto organic matter or as uraninite in sediment pore-waters (Anderson et al., 1989; Klinkhammer and Palmer, 1991; Cochran, 1992; Barnes and Cochran, 1993; Morford and Emerson, 1999; Bone et al., 2017). Regardless of the mechanism involved, studies of anoxic basins have shown that precipitation of U under anoxic to euxinic conditions preferentially enriches the sediments in ^{238}U (relative to ^{235}U), which lowers $^{238}U/^{235}U$ ratios in residual aqueous U(VI) (see review of Andersen et al., 2017). The positive fractionation imparted by U reduction contrasts with most traditional and non-traditional stable isotope systems where the oxidized species tend to be enriched in heavier isotopes. This peculiar behavior in U isotopes arises from the dominance in the total equilibrium isotopic fractionation of nuclear volume effect rather than vibrational (mass-dependent) control (Bigeleisen, 1996; Schauble, 2007; Abe et al., 2008).

The large isotopic fractionation during reduction of U (VI) to U(IV) causes the U isotopic composition of anoxic sediments to be highly fractionated relative to seawater. Along with the U burial rate in anoxic settings, the $\delta^{238}U$ value of seawater is largely controlled by the size of the anoxic sinks. An increase in the extent of oceanic anoxia will shift the seawater composition towards lower [U] and $\delta^{238}U$ values. Accordingly, the U isotopic composition of modern seawater can help constrain the extent of modern anoxia (Stirling et al., 2007; Weyer et al., 2008; Tissot and Dauphas, 2015; Andersen et al., 2017). A virtue of the uranium isotope system is that the residence time of U in the well-oxygenated modern ocean ($\tau \approx 400$ kyr) is much longer than the global ocean mixing time (~1–2 kyr), meaning that U concentration and isotopic composition in the open ocean are relatively uniform vertically and laterally. To first order, the U isotopic composition of carbonate and anoxic sediments that interacted with overlying seawater are expected to record global oceanic redox conditions, providing a means of assessing quantitatively the extent of ocean anoxia through time.

Shales were the first sediments used to estimate the U isotopic composition of ancient seawater (Montoya-Pino et al., 2010). A notable difficulty with these sediments is that a fraction of their U has a detrital origin, which requires a correction. Chemical tracers of detrital input, such as Al/U ratios, are commonly used to infer the U isotopic composition of the authigenic component (Asael et al., 2013). This correction can be significant and contributes to the uncertainty in paleoredox reconstructions. A second difficulty with the shale record is that the apparent isotopic fractionation in anoxic/euxinic settings is large and variable and it can be influenced by the efficiency of U transport to the sediments and deep-water renewal (Andersen et al., 2014; Noordmann et al., 2015; Andersen et al., 2018).

Marine carbonates provide an alternative and possibly more faithful and straightforward archive of seawater

$\delta^{238}U$ values through time. Indeed, modern primary carbonate precipitates are found to have a $\delta^{238}U$ composition that is close to that of seawater (Stirling et al., 2007; Weyer et al., 2008; Romaniello et al., 2013; Chen et al., 2018a, 2018b; Tissot et al., 2018), and the small detrital contribution can be minimized by partial dissolution of the carbonates in dilute acid. Based on the assumption that there is little fractionation between carbonates and seawater, several studies have used carbonates to track redox transitions during critical intervals such as at the Cambrian-Ordovician boundary, the end of the Sturtian Snowball Earth, and the Permian-Triassic boundary (Brennecka et al., 2011; Dahl et al., 2014, 2017, 2019; Azmy et al., 2015; Hood et al., 2016; Lau et al., 2016, 2017; Elrick et al., 2017; Jost et al., 2017; Song et al., 2017; Bartlett et al., 2018; Clarkson et al., 2018; Phan et al., 2018; White et al., 2018; Zhang et al., 2018a, 2018b, 2018c, 2019a, 2019b, 2020a, 2020c; Gilleaudeau et al., 2019; Tostevin et al., 2019; Cao et al., 2020; Cheng et al., 2020; del Rey et al., 2020; Li et al., 2020; Zhao et al., 2020). Most of these studies focused on variations in the U isotopic composition of carbonates during short time intervals to trace the expansion or contraction of anoxia in the oceans. A complication to the carbonate $\delta^{238}U$ paleoredox is that it is affected by diagenesis (see review in Zhang et al., 2020b), which can shift the $\delta^{238}U$ values of carbonates by ~+0.2‰ to +0.4‰ relative to seawater (Romaniello et al., 2013; Chen et al., 2018a; Tissot et al., 2018). Precipitation of abiotic (Chen et al., 2016, 2017) and biogenic (Chen et al., 2018b) carbonates can also induce a small shift in the U isotopic composition of carbonates relative to seawater (< +0.1‰). When available, calcitic brachiopod shells may be a better proxy for ambient seawater composition as they are more resistant to isotopic exchange with porewater during diagenesis (del Rey et al., 2020; Livermore et al., 2020). Regardless of these complications, carbonates have proven to be a useful sedimentary archive for reconstructing the extent of oceanic anoxia through time.

Earth's surface oxygenation was marked by two critical transitions known as the Great Oxidation Event (GOE) at ca. 2.43–2.06 Ga and the Neoproterozoic Oxygenation Event (NOE) at ca. 0.68–0.54 Ga (potentially starting as early as 0.8 Ga), which both saw dramatic changes in global surface environments (Holland, 2002; Bekker et al., 2004; Johnston et al., 2012; Thomson et al., 2015; Turner and Bekker, 2016; Gumsley et al., 2017). While most previous studies have focused on specific short intervals of Earth's history when significant change in Earth's surface redox state happened, the aim of the present work is to investigate how U concentrations and isotopic compositions of sediments responded to Earth's progressive oxygenation over the full temporal extent of carbonate sedimentary record and test the tenets of the U isotope paleoredox proxy. For that purpose, we use carbonates as they should represent the best archive of the uranium isotopic composition of seawater through time.

Taking clues from the modern U cycle, paleoredox reconstructions assume a near-constant U isotopic fractionation between oxidized U dissolved in seawater and reduced U deposited under anoxic conditions with organic-rich shales. The validity of this assumption can be directly tested by comparing the $^{238}U/^{235}U$ values in coeval shales and carbonates over broad geological timescales, in a similar manner to what has been done for $\delta^{13}C$ (organic and carbonate carbon) and $\delta^{34}S$ (sulfide and sulfate sulfur) proxies. Here, we report new $\delta^{238}U$ analyses of 95 Precambrian carbonates and combine these results with a compilation of literature data for carbonate and shale to test the assumption that the $\delta^{238}U$ values of shales are indeed fractionated relative to carbonates by a constant offset.

2. MATERIALS AND METHODS

2.1. Samples

In order to reconstruct the long-term redox evolution of the ocean, a large suite of marine carbonates (Table 1) was assembled and the U concentrations and isotopic compositions of 95 carbonate samples spanning the Archean to Neoproterozoic were measured and combined with previously published data (Brennecka et al., 2011; Dahl et al., 2014, 2017, 2019; Azmy et al., 2015; Hood et al., 2016; Lau et al., 2016, 2017; Elrick et al., 2017; Jost et al., 2017; Song et al., 2017; Bartlett et al., 2018; Chen et al., 2018a, 2018b; Clarkson et al., 2018; Herrmann et al., 2018; Phan et al., 2018; White et al., 2018; Zhang et al., 2018a, 2018b, 2018c, 2019a, 2019b, 2020a, 2020c; Gilleaudeau et al., 2019; Tostevin et al., 2019; Brüske et al., 2020a; Bura-Nakić et al., 2020; Cao et al., 2020; Cheng et al., 2020; Li et al., 2020; del Rey et al., 2020; Zhao et al., 2020). The age and detailed description of the geological settings can be found in the references provided in Table 1 and in Supplementary Materials. Most of the analyzed carbonate samples were deposited in shallow-marine settings above the storm (typically less than 15–40 m depth) and fair-weather-wave base (less than 5–15 m depth), and only two sample sets show no evidence for subaerial emergence and were likely deposited in a deeper environment. We avoided deep-water carbonate depositional settings, sediments with high organic carbon content, and thin carbonate beds and nodules in shales. Most of the sampled carbonate units are tens to hundreds of meters thick, contain little if any detrital material, and have sedimentary textures and structures indicating precipitation from seawater above the fair-weather-wave base. There are several reasons to expect that carbonate deposition in the Precambrian was dominantly restricted to shallow-marine settings and, after the Great Oxidation Event (GOE), was predominantly above the redoxcline:

(i) Export of carbonate to deep-water settings requires foraminifera and coccoliths and these did not evolve until the Phanerozoic, resulting in predominantly shallow-water carbonates in early Phanerozoic and Precambrian (*e.g.*, Holland and Zimmermann, 2000). The only mechanism by which carbonates were transported to deep waters in the Precambrian was through gravity flow deposition, and such slope/deep water deposits were relatively rare.

Table 1
Sample age and locality, Mn/Sr, Mg/Ca ratios, stable isotopic compositions and U concentrations and isotopic compositions of the carbonates measured in this study.

Sample	Rock Type	Age (Ga)	±	Mn/Sr	$\delta^{13}C$ carb (‰ V-PDB)	$\delta^{18}O$ (‰ V-PDB)	Reference*	Total carbonate[a] (wt%)	Mg/Ca[a]	[U][b] (ppb)	±	$\delta^{238}U$[c] (‰)	±	$\delta(^{234}U/^{238}U)$[d] (‰)	±
Fig Tree Group, Barberton Greenstone Belt, Swaziland Supergroup, South Africa															
78-FT-15	Dolostone	3.25	0.02	34.6	1.56	−13.13	1	38.16	0.41	171.6	1.5	−0.21	0.06	728.90	0.35
Woman Lake Group, Uchi Greenstone Belt, Canada															
78-WO-629	Limestone	2.87	0.01	271.2	1.18	−10.19	1	85.54	0.01	113.4	1.0	−0.31	0.03	52.02	0.19
78-WO-617G	Limestone	2.87	0.01	121.3	1.30	−8.80	1	87.24	0.01	108.4	0.9	−0.21	0.03	−6.62	0.24
78-WO-621	Limestone	2.87	0.01	64.8	0.20	−12.70	1	72.84	0.11	383.0	1.7	−0.03	0.04	−11.97	0.33
Confederation Lake	Limestone	2.87	0.01	181.3	1.30	−9.10	1	82.60	0.01	68.0	0.6	−0.69	0.03	175.66	0.37
Mosher Carbonate, Steep Rock Lake Group, Wabigoon Belt, Canada															
1977/43	Limestone	2.79	0.01	8.9	2.50	−9.00	1	84.07	0.02	62.0	0.7	−0.53	0.03	73.74	0.34
1977/43 rep1.										58.4	0.7	−0.54	0.03	65.69	0.34
1977/43 rep2.										67.3	0.7	−0.56	0.03	77.53	0.34
								Average		*62.5*	*0.4*	*−0.54*	*0.02*	*72.32*	*0.20*
1977/42	Limestone	2.79	0.01	2.5	2.00	−9.21	1	82.74	0.03	26.9	2.3	−0.42	0.06	290.78	0.38
Tumbiana Formation, Forstescue Group, Australia															
84-F-54.9	Limestone	2.73	0.01	293.0	−4.01	−18.77	2	51.00	0.02	74.3	0.7	−0.21	0.05	368.90	0.57
84-F-106	Limestone	2.73	0.01	140.1	−2.06	−8.34	2	37.23	0.08	162.0	1.5	−0.21	0.05	333.98	0.57
84-F-112.3	Limestone	2.73	0.01	705.6	−2.48	−18.43	2	32.96	0.06	142.3	1.3	−0.08	0.05	503.57	0.57
84-F-158.6	Limestone	2.73	0.01	303.9	−3.23	−18.74	2	37.64	0.03	84.8	0.8	−0.19	0.05	597.36	0.57
Klippan and Bothaville Formations, Vendersdorp Supergroup, South Africa															
79-VE-15	Limestone	2.72	0.01	14.6	−2.10	−19.60	2	34.04	0.05	233.6	2.0	−0.23	0.04	2111.19	0.28
79-VE-11c	Limestone	2.72	0.01	3.2	−3.19	−19.04	2	24.42	0.23	71.3	0.7	−0.01	0.11	3314.56	0.61
Gwanda Greenstone Belt, Zimbabwe															
78-SE-1b	Limestone	2.70	0.00	200.2	0.80	−9.60	1	84.33	0.01	22.8	0.3	−0.26	0.09	215.54	1.00
Yellowknife Supergroup, Slave Province, Canada															
HBA-J-224.2.74	Limestone	2.67	0.01	3.5	−5.70	−18.20	1	28.26	0.16	551.2	5.8	−0.43	0.04	424.08	0.30
HBA-J-147.4.74	Limestone	2.67	0.01	33.9	−14.37	−15.84	1	90.66	0.53	54.6	0.5	−0.18	0.08	10.48	0.43
Carawine Dolomite, Hamersley Group, Australia															
84-Ca-240	Dolomite	2.63	0.00	627.5	−0.30	−8.70	2	81.01	0.08	23.4	0.2	−0.42	0.06	357.05	0.70
84-Ca-114	Dolomite	2.63	0.00	831.7	−0.77	−5.83	2	77.00	0.47	374.6	1.1	−0.41	0.02	70.36	0.18
84-Ca-118.3	Dolomite	2.63	0.00	647.9	−0.10	−5.25	2	86.08	0.53	256.5	0.9	0.00	0.03	35.70	0.19
Gamohaan Formation, Campbellrand Subgroup, South Africa															
WB98 − 519.33	Calcite	2.52	0.00		−1.24	−8.00	3	74.29	0.01	83.9	0.7	−0.32	0.04	201.03	0.48
WB98 − 515.13	Calcite	2.52	0.00		−1.55	−8.39	3	60.55	0.02	800.4	2.5	−0.12	0.03	139.02	0.25
WB98 − 513.2	Calcite	2.52	0.00		−1.77	−8.46	3	63.56	0.02	361.9	1.9	−0.12	0.04	171.76	0.24
WB98 − 519.63	Calcite	2.52	0.00		−3.32	−7.09	3	66.50	0.04	173.5	1.5	−0.11	0.03	112.86	0.22
WB98 − 509.6	Calcite	2.52	0.00		−1.78	−8.62	3	62.70	0.02	47.6	0.4	−0.23	0.04	255.33	0.47
WB98 − 519.63 white	Calcite	2.52	0.00		−0.48	−6.93	3	66.22	0.01	40.3	0.4	−0.58	0.05	67.94	0.58
WB98 − 522.44	Calcite	2.52	0.00		−1.18	−8.49	3	74.56	0.02	41.9	0.4	−0.36	0.04	149.55	0.47
Itabira Group, Gandarela Formation, Brazil															
GA-2 white	Calcite	2.43	0.00	13.1–15.4	−0.60	−8.80	4	87.62	0.01	71.4	0.7	−0.72	0.05	216.75	0.36
GA-2 white rep1.										82.4	0.8	−0.75	0.04	158.69	0.32
GA-2 white rep2.										93.4	0.9	−0.78	0.04	103.78	0.32
								Average		*80.8*	*0.4*	*−0.75*	*0.03*	*155.67*	*0.19*
GA-1	Calcite	2.43	0.00	26.7	−0.40	−8.20	4	86.17	0.02	28.6	0.3	−0.82	0.12	−218.89	0.77
GA-4	Calcite	2.43	0.00	7.5	−1.00	−9.30	4	71.09	0.09	239.2	2.1	−0.76	0.05	193.88	0.35
GA-2 black	Calcite	2.43	0.00	13.1–15.4	−0.60	−8.80	4	76.18	0.05	165.6	1.4	−0.91	0.04	−259.23	0.26
Espanola Formation, lower Huronian Supergroup, Canada															
82-BL-2	Limestone	2.40	0.00	2.1	−1.29	−16.20	5	69.01	0.02	135.5	1.2	−0.29	0.03	1661.30	0.46
82-BL-5	Limestone	2.40	0.00	2.5	−1.24	−16.41	5	70.24	0.03	73.7	0.6	−0.18	0.04	1097.34	0.48

(*continued on next page*)

Table 1 (*continued*)

Sample	Rock Type	Age (Ga)	±	Mn/Sr	$\delta^{13}C$ carb (‰ V-PDB)	$\delta^{18}O$ (‰ V-PDB)	Reference*	Total carbonate[a] (wt%)	Mg/Ca[a]	[U][b] (ppb)	±	$\delta^{238}U$[c] (‰)	±	$\delta(^{234}U/^{238}U)$[d] (‰)	±
BL-S54-1697	Limestone	2.40	0.00	5.9	−1.46	−16.29	5	68.59	0.05	110.5	0.9	−0.31	0.04	2268.95	0.48
DM1722′	m. calcite	2.40	0.00	22.8	−2.10	−12.90	6	21.23	0.08	626.6	8.6	−0.35	0.04	426.64	0.30
DM2323′3″	Calcite	2.40	0.00	12.6	−1.50	−14.30	6	54.87	0.51	324.5	1.5	−0.33	0.02	373.11	0.19
Gordon Lake Formation, upper Huronian Supergroup, Canada															
PL-SA	Dolomite	2.31	0.00	123.6	6.20	−8.90	7	38.26	0.56	752.0	2.0	−0.27	0.02	305.45	0.18
PL-S	Dolomite	2.31	0.00		5.80	−9.40	7	33.33	0.58	602.1	2.2	−0.25	0.03	631.96	0.19
KN-S	Dolomite	2.31	0.00	4.6	8.20	−10.30	7	75.28	0.55	301.8	1.1	−0.21	0.02	168.53	0.19
Pretoria Group, Silverton Formation, South Africa															
Si-4	Dolostone	2.15	0.00	2.9	9.10	−7.40	8	75.56	0.53	107.3	0.5	−0.28	0.04	580.27	0.25
Mcheka Formation, Lomagundi Group, Zimbabwe															
SLD-11	Dolomite	2.10	0.00		11.60	−4.80	9	78.92	0.61	492.7	1.1	−0.32	0.02	63.71	0.18
Fecho do Funil Formation, Minas Supergroup, Minas Gerais, Brazil															
PC-5	Dolomite	2.10	0.00	61.3	7.40	−11.00	4	70.20	0.54	146.8	0.7	−0.29	0.04	274.62	0.25
Mistassini Group, Albanel Formation															
MI-10-1	Dolomite	2.10	0.00		0.30	−9.60	10	18.08	1.04	497.1	4.8	−0.35	0.04	277.34	0.25
D2-83-74	Limestone	2.10	0.00	1.1	1.23	−10.93	10	76.77	0.04	166.4	1.5	−0.50	0.03	129.34	0.18
D2-81-74	Limestone	2.10	0.00	0.7	1.46	−11.51	10	34.29	0.47	696.3	3.5	−0.29	0.03	155.90	0.20
D2-72-74	Limestone	2.10	0.00				10	20.53	0.84	273.7	2.4	−0.03	0.05	491.15	0.31
Upper Nash Fork Formation, upper Libby Creek Group, USA															
2000-3	Dolomite	2.05	0.00	1.8	1.50	−4.80	11	75.11	0.55	141.3	0.5	−0.55	0.02	57.58	0.20
Roberts Draw Formation and Estes Creek Formation, Black Hills, South Dakota															
B99.14	Calcite	2.00	0.00		−0.20	−9.80	11	79.76	0.51	524.2	0.9	−0.17	0.02	149.25	0.18
B99.11	Dolomite	2.00	0.00		1.30	−9.70	11	75.69	0.52	61.3	0.5	−0.42	0.06	1144.69	0.35
SD99.2-7	Dolomite	2.00	0.00		2.40	−11.70	11	78.85	0.52	193.9	0.5	−0.30	0.02	668.62	0.19
Snare Group, Basler Lake, NWT, Canada															
SN-1	Dolomite	1.97	0.00		2.52	−8.07	12	92.53	0.54	150.3	0.4	−0.42	0.02	182.15	0.18
Aluminium River Formation, Amer Group, Nunavut, Canada															
AMC14	Dolomite	1.93	0.00		4.27	−7.13	13	85.75	0.61	258.2	0.8	−0.44	0.03	−111.11	0.20
Watterson Formation, Hurwitz Group, Nunavut, Canada															
96-16-1	Dolomite	1.93	0.00	15.2	1.40	−9.50	14	83.92	0.57	71.2	0.6	−0.36	0.05	658.93	0.27
Cowles Lake Formation, Coronation Supergroup, NWT, Canada															
84-Co-19	Limestone	1.88	0.00	0.5	1.80	−13.14	5	56.43	0.09	152.1	1.3	−0.32	0.03	149.55	0.42
84-Co-20	Limestone	1.88	0.00	3.2	−1.83	−13.29	5	67.04	0.02	53.3	0.5	−0.32	0.05	504.63	0.57
84-Co-21	Limestone	1.88	0.00	4.4	1.40	−11.28	5	74.67	0.05	60.0	0.5	−0.35	0.04	533.07	0.55
Taltheilei Formation, Pethei Group, NWT, Canada															
TL 12	Dolomite	1.86	0.00		1.37	−8.01	12	58.57	0.56	217.3	1.0	−0.28	0.02	960.23	0.19
George Formation, Muskwa Assemblage, BC, Canada															
MUSQUA		1.60	0.00				15	53.42	0.15	122.3	1.1	−0.36	0.04	1346.94	0.48
Wallace, Helena, and Snowslip Formations, Belt Supergroup, MT, USA															
Base	Limestone	1.45	0.00				12	58.49	0.04	2649.2	4.4	−0.19	0.04	103.79	0.30
Upper1	Limestone	1.45	0.00				12	73.31	0.03	186.4	1.7	−0.24	0.04	290.59	0.27
B1-5	Limestone	1.45	0.00				12	36.51	0.16	336.9	3.3	−0.29	0.05	504.33	0.35
A1-5	Limestone	1.45	0.00				12	44.16	0.04	219.8	1.9	−0.40	0.04	574.68	0.26
Upper2	Limestone	1.45	0.00				12	71.00	0.06	191.7	1.6	−0.29	0.04	243.39	0.33
RP190	Limestone	1.45	0.00				12	67.45	0.02	77.3	0.9	−0.28	0.03	538.00	0.18
RP10	Limestone	1.45	0.00		−0.68	−10.46	12	62.13	0.02	45.4	0.4	−0.13	0.04	1371.70	0.47
RP 682	Limestone	1.45	0.00		2.08	−9.33	12	79.32	0.01	94.1	0.8	−0.57	0.04	418.22	0.28
RP 711	Limestone	1.45	0.00		1.33	−10.18	12	75.27	0.03	66.5	0.6	−0.51	0.03	492.84	0.37
RP 504	Limestone	1.45	0.00				12	74.70	0.02	205.9	1.5	−0.20	0.03	192.91	0.25

Sukhaya Tunguska Fm., Western Siberia															
GS4-448	Limestone	1.04	0.00		3.50	−6.86	16	87.16	0.01	39.2	0.4	−0.64	0.07	147.08	0.50
GS4-448 rep1.										49.5	0.5	−0.59	0.07	136.65	0.50
GS4-448 rep2.										51.7	0.5	−0.64	0.06	147.90	0.41
								Average		*45.4*	*0.3*	*−0.63*	*0.04*	*144.45*	*0.27*
GS4-401	Limestone	1.04	0.00	0.04	1.50	−6.61	16	75.30	0.04	127.6	1.1	−0.82	0.04	127.14	0.34
GS4-490	Limestone	1.04	0.00		3.75	−6.59	16	86.46	0.02	145.9	1.3	−0.79	0.04	76.57	0.27
GS4-478	Limestone	1.04	0.00		3.06	−6.64	16	87.22	0.05	77.7	0.7	−0.64	0.04	163.67	0.28
GS4-383	Limestone	1.04	0.00		1.14	−7.29	16	73.05	0.02	81.8	0.7	−0.61	0.04	217.05	0.55
Ymer Ø Group, Eleonore Supergroup, E. Greenland															
GR9-564	Limestone	0.81	0.01	0.01	5.33	−8.32	17, 18	84.23	0.00	1159.6	2.5	−0.64	0.04	56.45	0.19
GR9-564 rep1.										1216.2	1.3	−0.65	0.04	55.89	0.19
GR9-564 rep2.										1204.3	1.3	−0.65	0.04	56.36	0.19
								Average		*1204.2*	*0.9*	*−0.65*	*0.02*	*56.23*	*0.11*
GR9-178.6	Limestone	0.81	0.01		4.34	−9.30	17, 18	53.15	0.12	70.4	0.8	−0.18	0.12	413.28	0.77
GR9-148.3	Limestone	0.81	0.01	1.80			17, 18	65.34	0.05	38.9	0.4	−0.22	0.05	779.74	0.58
GR9-148.3 rep										36.7	0.3	−0.25	0.05	747.24	0.57
								Average		*37.6*	*0.3*	*−0.23*	*0.04*	*763.40*	*0.41*
GR9-131	Limestone	0.81	0.01	0.90	−0.86	−9.45	17, 18	73.72	0.02	406.0	1.7	−0.14	0.04	471.83	0.33
GR9-120.3	Limestone	0.81	0.01	0.67	−0.34	−9.98	17, 18	79.62	0.01	34.6	0.4	0.10	0.06	628.04	0.70
GR9-326	Limestone	0.81	0.01	0.02	4.98	−7.66	17, 18	86.78	0.01	132.3	1.0	−0.64	0.03	48.77	0.41
Elbobreen Fm., Polarisbreen Group, Svalbard															
G529-66	Limestone	0.73	0.00	0.64	2.51	−8.85	19, 20	67.20	0.04	289.4	2.6	−0.32	0.03	365.86	0.18
G529-77	Limestone	0.73	0.00	0.47	2.55	−8.71	19, 20	67.57	0.05	18.8	0.3	0.01	0.06	488.39	0.70
G529-68.1	Limestone	0.73	0.00	0.54	2.13	−9.07	19, 20	63.28	0.07	118.9	1.2	−0.18	0.04	402.62	0.48
G529-72.5	Limestone	0.73	0.00	0.36	−1.91	−8.67	19, 20	81.16	0.02	48.6	0.4	−0.11	0.04	431.07	0.55
Bed-Group 20, E. Greenland															
GR16-70	Limestone	0.73	0.00	0.83	−6.47	−8.25	21	45.73	0.12	293.2	2.5	−0.52	0.06	255.77	0.38
GR16-105.4	Limestone	0.73	0.00		−2.30	−7.26	21	74.57	0.01	127.6	1.1	−0.79	0.03	56.04	0.24
GR16-37.3	Limestone	0.73	0.00		−6.38	−4.24	21	38.89	0.73	373.4	2.3	−0.47	0.02	171.65	0.19
Rasthof Formation, Otavi Group, Namibia															
B036-20.0	Limestone	0.66	0.00		−0.80	−10.30	22	83.93	0.04	237.6	2.9	−0.14	0.03	201.14	0.18
B036-20.0 rep1.										289.3	3.1	−0.17	0.03	199.66	0.18
B036-20.0 rep2.										296.1	3.1	−0.19	0.03	194.75	0.18
								Average		*272.4*	*1.7*	*−0.16*	*0.02*	*198.51*	*0.11*
B036-7.9	Limestone	0.66	0.00		−1.80	−8.20	22	85.96	0.08	401.9	1.4	−0.21	0.04	395.52	0.24
B036-35.7	Limestone	0.66	0.00		−1.00	−6.90	22	81.62	0.03	66.1	0.4	−0.34	0.05	110.67	0.34
B036-3.4	Limestone	0.66	0.00		−2.20	−8.40	22	83.21	0.07	485.7	1.5	−0.13	0.04	315.02	0.33
B036-40.0	Limestone	0.66	0.00		−0.40	−6.20	22	84.02	0.04	377.0	1.5	−0.18	0.03	146.29	0.25
B036-12.0	Limestone	0.66	0.00				22	86.49	0.16	109.6	1.2	−0.27	0.03	591.37	0.41
B036-2.5	Limestone	0.66	0.00		−1.80	−6.80	22	85.33	0.16	235.6	1.8	−0.19	0.03	217.76	0.41
Maieberg Formation, Otavi Group, Namibia															
P4017.6.0	Dolostone	0.63	0.00		−2.98	−6.01	22	91.83	0.58	226.5	0.9	−0.33	0.02	251.59	0.19
P4017.16.1	Dolostone	0.63	0.00		−4.51	−7.79	22	76.71	0.55	193.7	0.6	−0.49	0.02	565.51	0.18
P4017.0.63	Dolostone	0.63	0.00		−3.10	−5.84	22	90.29	0.54	29.3	0.3	−0.15	0.08	555.85	0.43
Geostandard															
SDO-1	Black Shale	Devonian						*Average*		*42237.8*	*17.0*	*−0.07*	*0.01*	*−0.40*	*0.07*

*References for sample description Mn/Sr and stable isotope data: (1) Veizer et al. (1989); (2) Veizer et al. (1990); (3) Rouxel et al. (2005); (4) Bekker et al. (2003b); (5) Veizer et al. (1992); (6) Bekker et al. (2005); (7) Bekker et al. (2006); (8) Bekker et al. (2008); (9) Master et al. (2010); (10) Mirota and Veizer (1994); (11) Bekker et al. (2003a); (12) Hardisty et al. (2017); (13) Rainbird et al. (2010); Bekker and Eriksson (2003); (14) Aspler and Chiarenzelli (2002); (15) Ross et al. (2001); (16) Bartley et al. (2001); (17) Sønderholm and Tirsgaard, 1993); (18) Wörndle et al. (2019); (19) Fairchild and Hambrey (1995); (20) Halverson et al. (2018); (21) Herrington and Fairchild (1989); (22) Hoffman and Halverson (2008).

[a] Estimated from major element abundances determined on compacted powder pellets using scanning electron microscope (SEM).

[b] U concentrations in the digested carbonate fraction

[c] $\delta^{238}U\ (‰) = [(^{238}U/^{235}U)_{sample}/(^{238}U/^{235}U)_{CRM\text{-}112a} - 1] \times 1000$, where CRM-112a is a U standard.

[d] $\delta(^{234}U/^{238}U)\ (‰) = [(^{234}U/^{238})_{sample}/(\lambda_{238}/\lambda_{234}) - 1)] \times 1000$, where λ_{238} and λ_{234} are the decay constants of ^{238}U and ^{234}U, respectively, $\lambda_{238}/\lambda_{234} = (1.5513 \times 10^{-10})/(2.8220 \times 10^{-6}) = 5.4970 \times 10^{-5}$ (Cheng et al., 2013).

(ii) The carbonate compensation depth in Precambrian oceans was likely shallower due to higher pCO_2.
(iii) Once the atmosphere became oxygenated and the shallow portion of the water column contained dissolved oxygen, the steady-state redoxcline could not have been shallower than the well-mixed layer above the fair-weather wave-base where most of our carbonates were deposited.

To summarize, our Precambrian carbonates typically record shallow depositional settings, and those deposited after the GOE likely precipitated above the redoxcline.

The least-altered and best-preserved samples were identified based on a combination of petrographic features and an array of geochemical tracers sensitive to the extent of post-depositional alteration (*i.e.*, Mg/Ca, Mn/Sr, $\delta^{18}O$, and $\delta^{13}C$ values) (Veizer et al., 1989; Banner and Hanson, 1990). When exposed to meteoric waters during sea level lowstands, the oxygen isotopic composition ($\delta^{18}O$) of shallow-marine carbonates evolves towards lower values. The $\delta^{18}O$ values of our samples mostly range between −14 and −4‰, which is within the expected range for well-preserved Precambrian carbonates (Shields and Veizer, 2002). The $\delta^{13}C$ values also fall within the range of well-preserved Precambrian carbonates (Shields and Veizer, 2002), characterized by a value close to 0‰ during much of the Precambrian with the exception of anomalously high and variable $\delta^{13}C$ values during the early and late Proterozoic (2.35–2.0 Ga and 0.8–0.6 Ga). We did not adopt some of the criteria (*e.g.*, Mn/Sr and Mg/Ca ratios) used in some recent studies on uranium isotope systematics of Phanerozoic carbonates (*e.g.*, Dahl et al., 2014; Lau et al., 2016; Bartlett et al., 2018) to screen Precambrian carbonate samples because early in Earth's history most carbonate units were dolomitized shortly after deposition and have high Mn/Sr and Mg/Ca ratios, but preserve primary Sr isotopic values and I content (Veizer et al., 1989, 1990, 1992a, 1992b; Hardisty et al., 2017). Excluding dolomitic units would also leave large gaps in the carbonate archive. Instead, for some intervals, we have analyzed both limestones and dolostones to assess the effect of dolomitization on uranium isotopic ratios (see also the discussions in Herrmann et al., 2018; Zhang et al., 2020a, 2020b).

2.2. Methods

Samples provided as rock specimens were visually inspected, and veins and non-carbonate component (*e.g.*, sulfides) were trimmed off with a rock saw. The carbonates samples were then crushed into fine powder using an agate mortar and pestle, and the carbonate content was estimated from major element abundances determined on compacted powder pellets using a JEOL JSM-5800LV scanning electron microscope (SEM). The carbonate content was used to calculate the amount of acid to add to each sample to fully digest the carbonate fraction without leaching detrital phases (Tissot et al., 2018; Clarkson et al., 2020; Zhang et al., 2020b).

Approximately 1 g of carbonate powder was used for each sample analysis. We added just enough 1 M HCl to digest only 1% of the sample in order to remove the easily mobilized U, which could be of secondary origin (Kuznetsov et al., 2017). The remaining bulk carbonates were digested using just enough 1 M HCl to digest the carbonate fraction. The centrifuge tubes containing the powdered carbonates were placed on a shaking platform to allow the solids and acid to fully react. Once the reaction was completed, after ~24 hours, the tubes were centrifuged and the supernatants were pipetted out. The remaining insoluble residues were dried in a laminar flow hood using heat lamps for approximately one day. The weight loss was used to estimate the mass of carbonate digested, which is required to calculate U concentrations. In Table 1, we report U concentrations in the digested carbonate fraction (amount of U in the leachate divided by mass of carbonate dissolved).

After digestion, 20 µL (~0.1%) of the sample solution was taken, diluted 100-fold and used for U concentration measurement on a Neptune MC-ICP-MS. The U concentrations were used to calculate the amount of spike to add before column chemistry. The remaining liquid was then transferred into a clean Teflon beaker and spiked with the IRMM-3636 U double spike (49.51% ^{236}U and 50.46% ^{233}U; Verbruggen et al., 2008). Enough spike was added to obtain a U_{spike}/U_{sample} ratio of ~3%. After spiking, the samples were dried completely then redissolved in concentrated HNO_3 before dilution with 3 M HNO_3. Uranium purification was performed on 2 mL cartridges (length = 2.7 cm, diameter = 0.8 cm) of U-TEVA specific resin, following the procedure described in previous publications (Telus et al., 2012; Tissot and Dauphas, 2015; Tissot et al., 2018). In brief, the resin was cleaned with 40 mL of 0.05 M HCl and conditioned with 10 mL of 3 M HNO_3. The digested samples were loaded onto the column in ~5 mL of 3 M HNO_3 and matrix elements were removed with 30 mL of 3 M HNO_3. The resin was converted with 5 mL of 10 M HCl. Thorium was eluted in 12 mL of 5 M HCl. Uranium was finally eluted in 32 mL of 0.05 M HCl. All samples were purified twice through the column chemistry to ensure full removal of matrix elements. Following chemical separation, the U cuts were dried down completely, taken back in 0.4 mL of HNO_3-H_2O_2 (1:1), and dried again before being re-dissolved in concentrated HNO_3, evaporated to near dryness, and taken back in 0.3 M HNO_3 for isotopic analysis.

All U isotopic analyses followed the protocol detailed in previous work of our group (Tissot and Dauphas, 2015; Tissot et al., 2017, Tissot et al., 2017) and were performed on the ThermoFinnigan Neptune MC-ICP-MS upgraded to Neptune Plus specifications (*i.e.*, with a jet pump installed) at the Origins Laboratory of the University of Chicago. Jet sample and X-skimmer cones were used in combination with an Aridus II desolvating nebulizer. The measurements were performed in low-resolution mode, using a static cup configuration and comprised 60 cycles of 4.194 s integration time each (see Tissot and Dauphas, 2015 for details). The measurements were performed on ~8 mL of solution with U concentrations between 20 and 30 ppb. The instrument sensitivity was ~1.5 V/ppb on ^{238}U with a 10^{11} Ω resistance amplifier and a 100 µl/min

nebulizer. Baseline and gain calibrations were performed daily. Isotope mass fractionation introduced during chemical separation and mass spectrometry was corrected for using the $^{233}U/^{236}U$ double-spike IRMM-3636. The data reduction methodology is described in detail in Tissot and Dauphas (2015). The sample measurements were bracketed by measurements of the CRM-112a standard spiked with IRMM-3636 with a spike/standard ratio similar to that of the samples. The $^{238}U/^{235}U$ ratios are reported using the δ notation in per mil units as,

$$\delta^{238}U(‰) = [(^{238}U/^{235}U)_{sample}/(^{238}U/^{235}U)_{CRM-112a} - 1] \times 1000. \quad (1)$$

The $^{234}U/^{238}U$ ratio is reported as a departure from secular equilibrium,

$$\delta(^{234}U/^{238}U) = [(^{234}U/^{238}U)_{sample}/(\lambda_{238}/\lambda_{234}) - 1]] \times 1000, \quad (2)$$

where λ_{238} and λ_{234} are the decay constants of ^{238}U and ^{234}U, respectively, and $\lambda_{238}/\lambda_{234} = (1.5513 \times 10^{-10})/(2.8220 \times 10^{-6}) = 5.4970 \times 10^{-5}$ (Cheng et al., 2013). The uncertainties are calculated based on the reproducibility of the CRM-112a standard measurements that bracketed the sample solution analyses and are reported as 95% confidence intervals.

3. RESULTS

We repeatedly processed (n = 24) and measured the U isotopic composition of geo-standard SDO-1 (a Devonian black shale) and found an average value of −0.07 ± 0.008‰ (2SD, each was measured 4–8 times in different sessions), which agrees well with previously published data for the same geo-standard of −0.08 ± 0.03‰ (Tissot and Dauphas, 2015). Several samples (with different ages) were replicated multiple times, from sequential dissolution to U isotope analysis. The U concentrations and isotopic compositions agree well between the replicate analyses (see Table 1). These measurements show that our data are reproducible and do not suffer from any obvious analytical bias.

Using the two-step leaching protocol described in Section 2.2, we measured U concentrations and isotopic compositions of carbonate samples (n = 95) ranging in age from 0.63 to 3.25 Ga. The first leaching step, aimed at removing easily mobilized U, released only 1 % of the total U during digestion of carbonate. Because of the low U concentrations in the Precambrian carbonates, large sample masses were used (typically 1 g) to provide sufficient U (typically ~20–200 ng) for $\delta^{238}U$ measurement with a precision of ~±0.05‰. The results are presented in Figs. 1 and 2, along with literature data (see references listed in Section 2.1 and Supplementary Table 1), and good agreement is observed for samples of similar age. Note that the data for carbonates with ages between 2.72 and 2.6 Ga from Wang et al. (2018) were excluded from this compilation because these samples display both high U concentrations (1.61 ppm on average) and Al/U ratios that are higher than average Al/U ratios in basalts and granites (Asael et al., 2013), indicating that the U budget in these samples is overwhelmed by detrital U.

We calculated average, median, and mode of U concentrations and $\delta^{238}U$ values of carbonates spanning different time intervals (before 2.43 Ga = preGOE; between 2.43 and 2.06 Ga = GOE; between 2.06 and 0.8 Ga = postGOE-preNOE; between 0.8 and 0.68 Ga = ruNOE = ramp up to NOE; between 0.68 and 0.54 Ga = NOE; 0.54 Ga to present = postNOE) and ran two-sided student *t*-tests to evaluate if these quantities changed significantly across consecutive time intervals. The average U concentration in preGOE carbonates is 209 ± 58 ppb (n = 64, median = 155 ppb, mode = 230 ppb), while the average of carbonates spanning the GOE is 323 ± 123 ppb (n = 17, median = 274 ppb). Carbonates deposited in postGOE-preNOE have an average [U] of 243 ± 45 ppb (n = 159, median = 160 ppb,

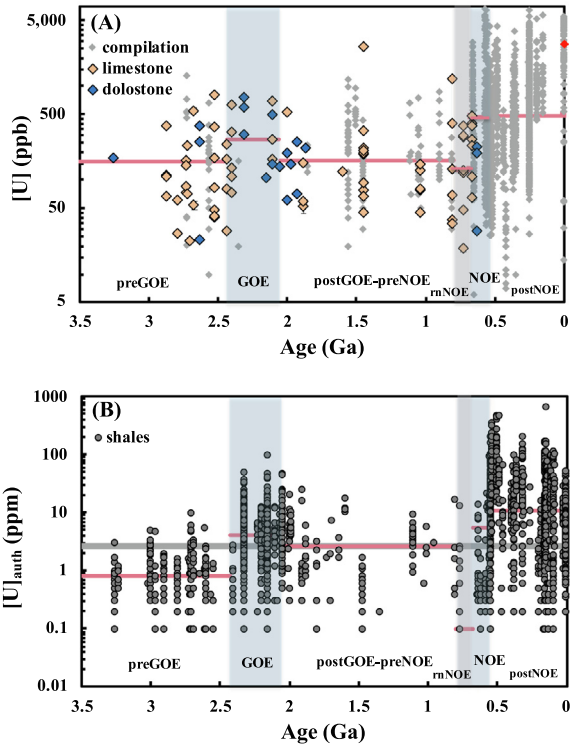

Fig. 1. (A). [U] in carbonates through time. [U] data measured in this study (orange diamonds = limestones; blue diamonds = dolostones) are for the leached carbonates fractions (U per unit mass of carbonate dissolved; see detail in Section 2.2). Grey diamonds are [U] literature data (see compilation in Supplementary Table 1). The red bars are the median uranium concentrations of carbonates in the six intervals of 3.25–2.43 Ga (preGOE), 2.43–2.06 Ga (GOE), 2.06–0.8 Ga (postGOE-preNOE), 0.8–0.68 Ga (ruNOE, ramp up to NOE), 0.68–0.54 Ga (NOE), and 0.54 Ga-present (postNOE). The large red dot is the median modern value. (B). $[U]_{auth}$ in shales through time ($[U]_{auth} = [U]_{total}-[Th]/3$ with [U] and [Th] in ppm). Note that [U] in carbonates and shales are displayed in different units (ppb vs. ppm). Shale data are from Partin et al., 2013a. The average [U] in the continental crust is indicated by the grey line at 2.7 ppm (Taylor and McLennan 1985). The red lines are the medians of the authigenic uranium concentrations in shales during the same six intervals as defined for the carbonate data.

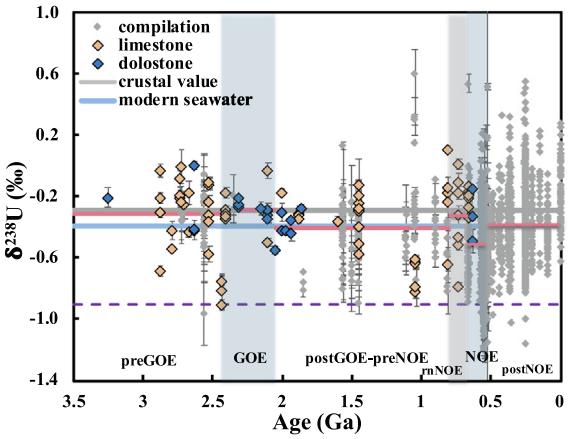

Fig. 2. $\delta^{238}U$ in carbonates through time. $\delta^{238}U$ data measured in this study on leached carbonates fraction are displayed as orange diamonds for limestones and blue diamonds for dolostones. For both [U] and $\delta^{238}U$, the data shows no systematic difference between dolostones and limestones in the Precambrian. Grey diamonds are literature data (see Supplementary Table 1). $\delta^{238}U$ of the continental crust (-0.29 ± 0.03‰) and modern seawater (-0.392 ± 0.005‰, Tissot and Dauphas 2015) are shown for comparison. The red lines are the median uranium isotopic composition of carbonates in the same six intervals as shown in Fig. 1. The purple dashed line shows the first-order expected $\delta^{238}U$ value (-0.9‰) of carbonates and seawater in a steady-state ocean if the uranium oceanic sink is predominantly anoxic (the U fraction going into anoxic sediment is close to 100%). Contrary to expectations, carbonates show $\delta^{238}U$ values similar to those of the continental crust and riverine runoff. These results are inconsistent with the view that the U isotopic composition of Precambrian seawater simply reflects the areal extent of anoxic sediments in the past.

mode = 120 ppb) (Fig. 1A). No significant difference in U concentration is detected for either preGOE and GOE, or GOE and postGOE-preNOE time intervals (*p*-values of 0.09 and 0.21, respectively). Shales show a clear increase in their U concentrations across the GOE (Partin et al., 2013a, see also Fig. 1B).

Carbonates deposited in ruNOE (0.8–0.68 Ga) have an average [U] of 181 ± 126 ppb (n = 7, median = 128 ppb). Carbonates deposited during the NOE (0.68–0.54 Ga) show a marked increase in U concentration to an average value of 952 ± 155 ppb (n = 410, median = 469 ppb, mode = 300 ppb). Carbonates deposited after the NOE and through the present have an average [U] of 901 ± 64 ppb (n = 1233, median = 486 ppb, mode = 240 ppb) (Fig. 1A). Statistical tests show that carbonates deposited before the NOE have significantly lower U concentrations than those deposited during the NOE or after (*p*-values of 0.30, 2×10^{-11}, and 0.55 for 2.06–0.8 Ga postGOE-preNOE *vs.* 0.8–0.68 Ga ruNOE; ruNOE *vs.* 0.68–0.54 Ga NOE, and NOE *vs.* 0.54–0 Ga postNOE comparisons, respectively). The significantly different average and median U concentrations in carbonates deposited before and after the NOE indicate that the U seawater cycle and reservoir size changed dramatically during the NOE.

There is no clear trend in the $\delta^{238}U$ value of carbonates across the GOE (Fig. 2) with *t*-tests yielding *p*-values of 0.11, 0.0003 and 0.07 for comparisons between preGOE/GOE, GOE/postGOE-preNOE and preGOE/postGOE-preNOE respectively. The preGOE samples have an average $\delta^{238}U$ value of -0.34 ± 0.06‰ (n = 59, median = -0.31‰, mode = -0.35‰), which is within error identical to the crustal value of -0.29 ± 0.03‰ (Tissot and Dauphas, 2015). The samples deposited during the GOE give an average $\delta^{238}U$ value of -0.28 ± 0.05‰ (n = 17, median = -0.29‰), and the postGOE-preNOE carbonates give an average $\delta^{238}U$ value of -0.40 ± 0.04‰ (n = 159, median = -0.41‰, mode = -0.36‰). Note that the $\delta^{238}U$ values of our Archean and mid-Proterozoic carbonates agree well with the recently published data from Brüske et al. (2020a), Wang et al. (2020) and Gilleaudeau et al. (2019). Although the postGOE-preNOE average and median $\delta^{238}U$ values are closer to the modern seawater value of -0.40‰ (Tissot and Dauphas, 2015) than those of the Archean carbonate samples, the two-sided student *t*-tests *p*-values between preGOE and postGOE-preNOE is 0.07, which shows no significant difference between these two intervals.

The ruNOE carbonates give an average $\delta^{238}U$ value of -0.34 ± 0.25‰ (n = 7, median = -0.32‰), while NOE and postNOE carbonates have average $\delta^{238}U$ values of -0.53 ± 0.03‰ (n = 393, median = -0.51‰, mode = -0.34‰) and -0.37 ± 0.01‰ (n = 1147, median = -0.39‰, mode = -0.37‰), respectively. The p-values of the statistical tests for comparison between postGOE-preNOE/ruNOE, ruNOE/NOE and NOE/-postNOE are 0.57, 0.12 and 7×10^{-21}, respectively. The statistical test results confirm that the U oceanic cycle was affected by the NOE (~0.54 Ga).

We have also compared the Precambrian dolostone compositions (shown in blue diamonds in Figs. 1 and 2) with those for limestone samples of the same ages (shown in orange diamonds in Figs. 1 and 2). Both [U] and $\delta^{238}U$ values show no significant systematic difference between dolostone and limestone samples (Figs. 1 and 2). In addition, we show in Fig. S1 the histograms of [U] and $\delta^{238}U$ values of shallow-marine and deep-marine carbonates in our sample set, and we find that there is no difference in [U] and $\delta^{238}U$ values between the two groups, with the caveat that the number of deep-marine carbonates measured in the present study is only 5.

The [U] and $\delta^{238}U$ values of carbonates are also plotted in Fig. 3A, color-coded to represent the same six intervals shown in Figs. 1 and 2. The distributions of the U data ([U] and $\delta^{238}U$) also suggest that except for the dramatic change recorded in carbonates spanning the NOE, there is no clear change prior to that time.

A possible concern is that given the low authigenic U concentration in Precambrian carbonates, they could be more easily disturbed by a detrital component than those deposited during the Phanerozoic. We find large $\delta(^{234}U/^{238}U)$ excesses in carbonate (Fig. 4) that do not correlate with $\delta^{238}U$ values (Fig. 5). As discussed below (Section 4.1), these ^{234}U excesses are thought to be due to recoil effects from detrital grains into carbonates, and they would be small if significant amounts of detrital U had been digested during leaching. As shown in Fig. 3A, we also do

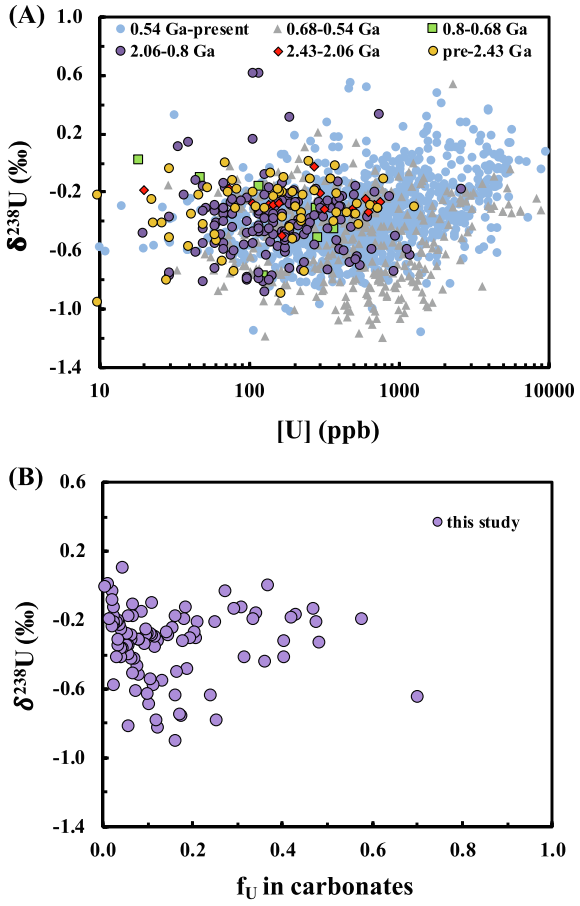

Fig. 3. (A). $\delta^{238}U$ *vs.* [U] in carbonates. Data are from this study and literature (see Supplementary Table 1). The distribution of the U data clearly shows that there are differences in the U oceanic cycle and reservoir size before and after NOE (~0.54 Ga), while differences among other time intervals are not clear based on the current dataset. (B). $\delta^{238}U$ *vs.* U fraction in carbonates (f_U). Neither $\delta^{238}U$ *vs.* [U], nor $\delta^{238}U$ *vs.* f_U show any correlation that point to contamination by a detrital component.

not see any correlation between [U] and $\delta^{238}U$ values of carbonates. We find no correlation neither between $\delta^{238}U$ values and the fraction of bulk U that is in the carbonate fraction (the rest is in the detrital fraction; assumed to have a composition close to that of the upper continental crust) (Fig. 3B). If the carbonates were contaminated by detritus through leaching in the laboratory or fluid circulation in sediments, one would expect to find mixing relationships in these diagrams. At lower [U] and higher f_U, $\delta^{238}U$ would tend to be more negative (closer to a putative anoxic ocean value), while at higher [U] and lower f_U, $\delta^{238}U$ would tend to be closer to the crustal value. No such correlation is found. To summarize, the effect of contamination by detrital U is most likely small and cannot account for the fact that most Precambrian carbonates have near-crustal $\delta^{238}U$ values.

We report in Table 1 and Fig. 4 the $\delta(^{234}U/^{238}U)$ values of our old carbonate samples. Most of the $\delta(^{234}U/^{238}U)$ values of our old carbonate samples deviate from secular equilibrium, with one sample displaying a value of ~+3500‰.

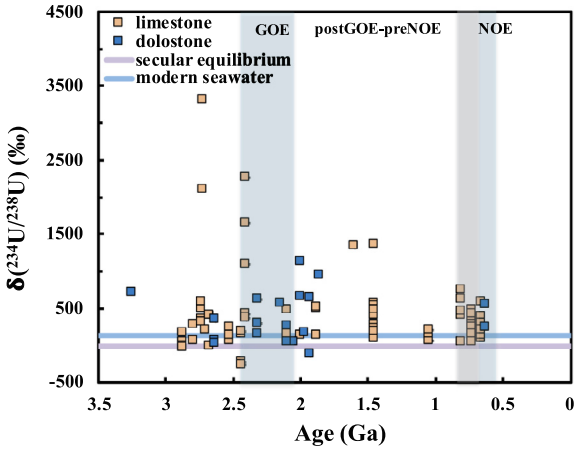

Fig. 4. $\delta(^{234}U/^{238}U)$ in Precambrian carbonates. Symbol colors as in Fig. 1. The purple horizontal line shows the secular equilibrium value (0‰), and the blue line shows the modern seawater value of ~145‰ (*e.g.* Ku et al., 1977; Chen et al., 1986; Andersen et al., 2010). Many of the $\delta(^{234}U/^{238}U)$ values of the carbonates measured in this study are much larger than the seawater value, suggesting that these excesses cannot be simply explained by post-depositional alteration by seawater alone. They most likely reflect recoil of ^{234}U into the carbonate fraction from the detrital fraction (see Fig. 6 and main text for details).

4. DISCUSSION

4.1. Excess $\delta^{234}U$ in ancient carbonates

As ^{234}U is the decay product of ^{238}U, carbonates that behaved as a closed systems for more than ~1.5 Myr (six times the half-life of ^{234}U, $t_{1/2} = 245,620$yr; Cheng et al., 2013) should be characterized by $\delta(^{234}U/^{238}U)$ values of ~0 (*i.e.*, $^{234}U/^{238}U$ activity ratio of 1) corresponding to secular equilibrium. Deviation from secular equilibrium indicates that some sort of open-system behavior affected the carbonate fraction. In modern marine sediments, and in particular carbonates, deviation from secular equilibrium is the result of incorporation of seawater U, which, in the modern ocean, has a $\delta(^{234}U/^{238}U)$ value of ~+145‰ (*e.g.* Ku et al., 1977; Chen et al., 1986; Andersen et al., 2010). This process cannot explain the $\delta(^{234}U/^{238}U)$ values of the Precambrian carbonates in this study as they display ^{234}U enrichments that are much greater than the modern seawater value (Fig. 4). The $\delta(^{234}U/^{238}U)$ values of Precambrian carbonates show no correlation with either [U] concentration or $\delta^{238}U$ (Fig. 5), suggesting that the factor causing excess in ^{234}U is unrelated to the processes that control their [U] and $\delta^{238}U$ values.

The excess in ^{234}U observed in old carbonates is most likely caused by alpha-recoil from the detrital fraction (with relatively high U concentration), whereby the daughter nuclides are implanted in the carbonate fraction (with low U concentration) in sedimentary rocks (Henderson et al., 2001). For old sedimentary rocks, the rate of gain of ^{234}U due to alpha-recoil will eventually equal the rate of decay of excess ^{234}U; the activity ratio at this equilibrium can be calculated as (modified from Henderson et al., 1999 for porewater),

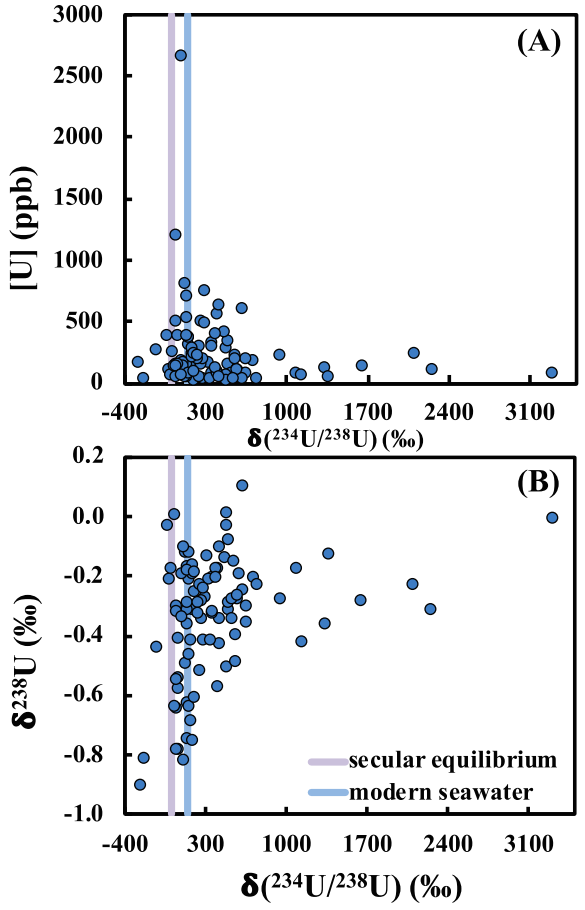

Fig. 5. (A). [U] *vs.* $\delta(^{234}U/^{238}U)$ and (B) $\delta^{238}U$ *vs.* $\delta(^{234}U/^{238}U)$ in the Precambrian carbonates measured in this study. The lack of correlation between these data suggests that the factor responsible for the $\delta(^{234}U/^{238}U)$ excesses in the sample had no impact on their [U] and $\delta^{238}U$ values.

$$\left(\frac{^{234}U}{^{238}U}\right) = \frac{r^3 - (r-\alpha)^3}{4r^3} \times \frac{U_{detritus} \times f_{detritus}}{U_{carbonate} \times f_{carbonate}} + 1, \quad (3)$$

where r is the effective radius of detrital grains in the sediment, α is the alpha-recoil distance of ^{234}Th (initial decay product of ^{238}U that decays in 24.1 day into ^{234m}Pa and then ^{234}U, $\alpha \approx 0.1$ μm, DePaolo et al., 2003) in silicates. The first term on the right side of the equation represents the volume fraction of daughter ^{234}U that will be expelled from the detrital grain into another grain (Bourdon et al., 2003). $U_{detritus}$ and $U_{carbonate}$ are the uranium concentrations in detrital and carbonate fractions, respectively; $f_{detritus}$ and $f_{carbonate}$ are the mass fractions of detritus and carbonate in the rock, respectively. The second term on the right side ($U \times f$) is the ratio of the U mass fractions in the detritus and carbonate. Larger excess of ^{234}U can be produced with finer detrital grain sizes (r), larger differences in U concentration ($\frac{U_{detritus}}{U_{carbonate}}$) and/or mass fractions ($\frac{f_{detritus}}{f_{carbonate}}$) between detritus and carbonates in the sediment. We plot the $\delta(^{234}U/^{238}U)$ values of our old carbonates as a function of ($\frac{U_{detritus} \times f_{detritus}}{U_{carbonate} \times f_{carbonate}}$) (Fig. 6) to check if the excess of $\delta(^{234}U/^{238}U)$ can be explained by the alpha-recoil effect

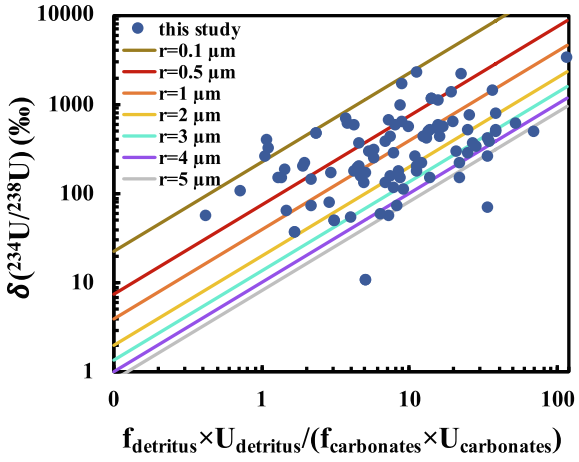

Fig. 6. $\delta(^{234}U/^{238}U)$ value in the carbonates measured in this study as a function of the ratio of U mass fractions in detritus and carbonate. The different lines correspond to predicted excesses due to alpha-recoil for different effective detritus grain sizes (r) (see Section 4.1 for details). The $\delta(^{234}U/^{238}U)$ value of our Precambrian carbonates show a broad correlation with the calculated index ($\frac{U_{detritus} \times f_{detritus}}{U_{carbonate} \times f_{carbonate}}$) of each sample, and the dispersion in the data can be explained by different detrital grain sizes, suggesting that the ^{234}U excesses observed in the carbonates were most likely caused by the alpha-recoil effect from the detrital fraction of the sediments.

(*i.e.*, a net transfer of $^{234}Th/^{234}U$ from detrital grains to carbonate in the rocks, Henderson et al., 2001). [U] in the continental crust (2.7 ppm; Taylor and McLennan, 1985) is used to represent $U_{detritus}$ and the measured [U] of each Precambrian carbonate in this study is $U_{carbonate}$. The carbonate mass fraction, $f_{carbonate}$, is estimated from major element abundances using a scanning electron microscope (Table 1). As seen in Fig. 6, the $\delta(^{234}U/^{238}U)$ value of our Precambrian carbonates broadly correlates with the calculated index ($\frac{U_{detritus} \times f_{detritus}}{U_{carbonate} \times f_{carbonate}}$) of each sample, the predicted correlation being modulated by grain size. This observation strengthens our interpretation that excess ^{234}U observed in ancient carbonates most likely comes from alpha-recoil and implantation from the detrital fraction into the carbonate fraction of ^{234}Th (and its decay product ^{234}U). This also confirms that the leaching protocol applied only releases U from the carbonate fraction and does not leach the detrital fraction in our rock samples, as any dissolution of the detritus would significantly decrease $\delta(^{234}U/^{238}U)$ and bring the values closer to the secular equilibrium value of ~0‰.

4.2. U concentration and isotopic records through time

The basis for using the U isotopic composition of either shales or carbonates to reconstruct seawater paleoredox conditions is that, at steady-state, the overall isotopic composition of U sinks (anoxic and others) must be equal to that of the riverine input, which is similar to that of the continental crust (−0.29‰; Stirling et al., 2007; Tissot and Dauphas, 2015; Andersen et al., 2016). At steady-state, the mass balance equation takes the form,

$$\delta U_{Input} = f \times \delta U_{anoxic} + (1-f) \times \delta U_{non\text{-}anoxic}, \quad (4)$$

where δU_{Input} is the U isotopic composition of the sources of U to the oceans, typically taken to be the modern river value of −0.26‰, f is the fraction of U removed to anoxic sinks (a measure of the extent of oceanic anoxia), and $\delta^{238}U_{non\text{-}anoxic}$ is the U isotopic composition of all non-anoxic sinks generally assumed to be negligibly fractionated from seawater. To calculate f from either carbonate (taken as a proxy for seawater, i.e. $\delta^{238}U_{non\text{-}anoxic}$) or organic-rich shale ($\delta^{238}U_{anoxic}$) values, it is usually assumed that the U isotopic composition of the anoxic sink is systematically shifted relative to seawater (SW) by a constant offset of $\Delta_{SW}^{anoxic} \simeq +0.6‰$ (the exact magnitude depends on the efficiency of U transport into pore-water and deep-water renewal; Andersen et al., 2014; Noordmann et al., 2015),

$$f = \frac{\delta U_{River} - \delta U_{SW}}{\delta U_{anoxic} - \delta U_{SW}} = \frac{\delta U_{River} - \delta U_{Carbonate}}{\Delta_{SW}^{anoxic}} = \frac{\delta U_{River} - \delta U_{Shale} + \Delta_{SW}^{anoxic}}{\Delta_{SW}^{anoxic}} \quad (5)$$

If the oceans were completely oxic and the anoxic sink was negligible, seawater would have the isotopic composition of the source (near-crustal), anoxic sediments would be shifted by ~+0.6‰ relative to the crust, and carbonates would have a near-crustal U isotopic composition. Conversely, if almost all U went into the anoxic sink, anoxic sediments would have the U isotopic composition of the source (near-crustal), and seawater and carbonates would be shifted by ~−0.6‰ relative to the crust. The current dataset of $\delta U_{Carbonate}$ values combined with previously published δU_{Shale} data allow us to evaluate one of the major tenets of the U isotope paleoredox proxy that the fractionation $\Delta_{SW}^{anoxic} \simeq +0.6‰$ documented in modern environments is applicable to the past.

In Figs. 1 and 7, we compare the U concentrations and $\delta^{238}U$ values of carbonates, shales, and iron-rich rocks. The disappearance of detrital uraninite at the GOE and the drastic change in U concentration of carbonates at the NOE, and of shales during the GOE and NOE imply that the redox cycle of U must have been drastically different in the Archean and Proterozoic relative to the present one. The $\delta^{238}U$ values of carbonates and shales deposited before ~2.43 Ga are largely indistinguishable, both defining averages that correspond to the crustal value (Fig. 7A). After the GOE, the two records start diverging as many shales display elevated $\delta^{238}U$ values (Asael et al., 2013; Kendall et al., 2015; Yang et al., 2017; Mänd et al., 2020) relative to carbonates of similar age (this study; Gilleaudeau et al., 2019; Fig. 7A). According to the isotope mass-balance outlined above and in previous publications (*e.g.*, Montoya-Pino et al., 2010; Brennecka et al., 2011; Tissot and Dauphas, 2015; Lau et al., 2016, 2017; Andersen et al., 2017), if a steady-state U seawater cycle existed and was dominated by anoxic settings in the Archean, one would expect Archean seawater and therefore carbonates to have a $\delta^{238}U$ value lower than the crust, possibly approaching −0.9‰. During the GOE and after the NOE, the $\delta^{238}U$ value of carbonates should have shifted towards the modern $\delta^{238}U$ value of −0.4‰ as the areal extent of anoxic settings shrank, and other sinks started to influence the mass-balance (Fig. 7B). Instead, we find that the U isotopic composition of carbonates did not change significantly through the Precambrian (Figs. 2 and 7A). Below, we explore two possible explanations as to why Archean and Proterozoic carbonates have similar U isotopic composition as continental runoff and Archean shales. We first focus on the residence time of U in the Precambrian oceans and ocean mixing timescale and show that they could have been much closer than in the modern ocean. We then discuss non-uniformitarian U isotopic fractionation during deposition of Precambrian black shales that might be responsible for the lack of a clear offset between black shale and carbonate U isotope records.

4.3. Residence time for U in Archean and Proterozoic oceans

In the modern oxic ocean, U is highly soluble as uranyl carbonate complexes (Langmuir, 1978; Dong and Brooks, 2006; Endrizzi and Rao, 2014; Maloubier et al., 2015). Its residence time of ~400 kyr (Ku et al., 1977; Chen et al., 1986; Dunk et al., 2002) greatly exceeds the mixing timescale of the oceans (~1 kyr, Siberlin and Wunsch, 2011; Khatiwala et al., 2012), meaning that the U content and isotopic composition of modern seawater is largely uniform and one can reliably assess the global mass-balance of U in the ocean among oxic, suboxic, carbonate, and anoxic sinks. In the Archean, seawater had much lower U concentration than in the modern ocean, and anoxic settings were much more extensive. It is thus likely that the residence time of U dissolved in seawater was much shorter. If the residence time of U was similar to the mixing timescale of the oceans, the U concentration and isotopic composition of the oceans would have been heterogeneous, which would have important consequences for interpretation of the U isotopic mass-balance of ancient carbonates and organic-rich shales.

To get a sense of how the U residence time could have been different in the past oceans compared to the modern value ($\tau \sim 400$ kyr), we have estimated the residence time of uranium for different extent of anoxia. The residence time is given by,

$$\tau = \frac{M_{sw}[U]_{sw,t}}{F_{in}}, \quad (6)$$

where M_{sw} is the mass of the oceans, $[U]_{sw,t}$ is the seawater U concentration at time t, and F_{in} is the U input flux into the ocean. The mass of the oceans M_{sw} did not change much since the Archean (presumably within a factor of 2; Pope et al., 2012; Korenaga et al., 2017). The input flux and U inventory of seawater could have changed more dramatically, and we examine below how the residence time of U could have been affected. These changes are assessed by examining the composition of chemical sediments, which indirectly record the composition of seawater from which they derive.

We estimate $[U]_{sw,t}$ and F_{in} in Eq. (6) based on an oceanic mass-balance model modified from Reinhard et al. (2013) and Sheen et al. (2018). At steady-state, the flux of

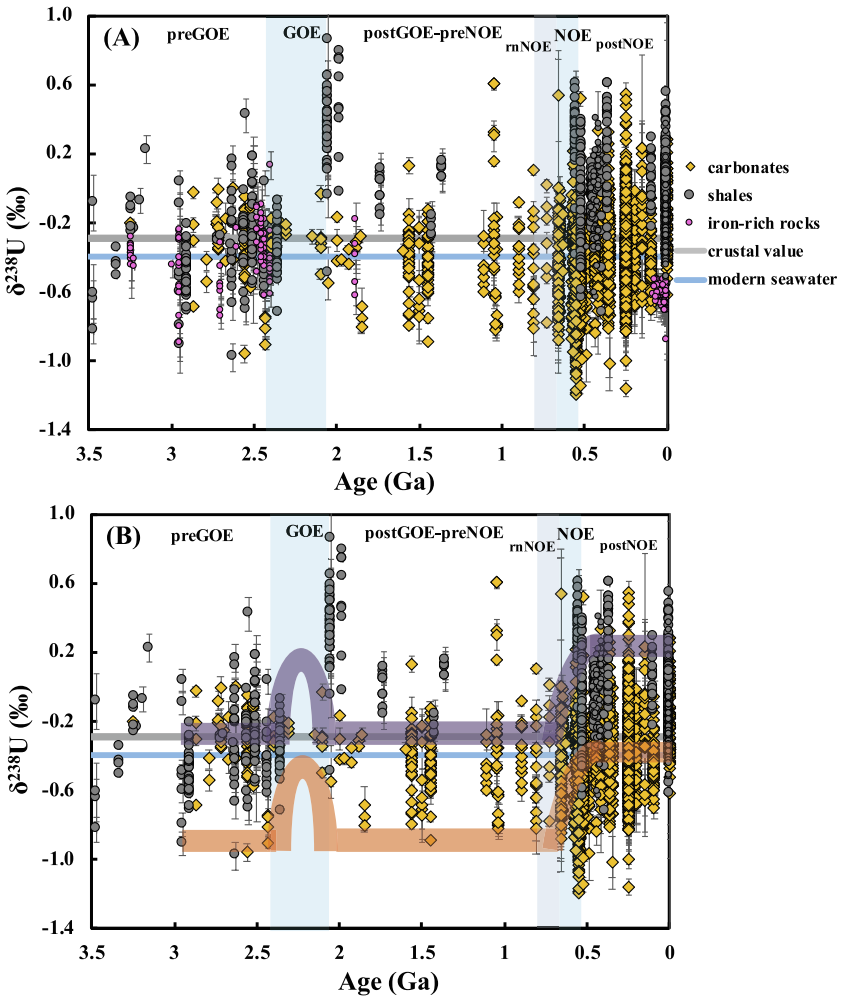

Fig. 7. (A). $\delta^{238}U$ in carbonates, shales, and iron-rich sedimentary rocks through time. $\delta^{238}U$ in carbonates are from this study and the literature (as in Figs. 1 and 2). $\delta^{238}U$ values for shales and iron-rich sedimentary rocks are from the literature (see compilation in Supplementary Table 1). If no $\delta^{238}U_{auth}$ were reported, the data were all corrected for detrital contribution using the method described in Asael et al., 2013. Samples with Al/U ratio larger than the detrital ratio were excluded from this figure. (B). The two broad bands illustrate the expected $\delta^{238}U$ trends in carbonates and shales under the assumption of constant offset between anoxic sinks and seawater (which is based on our current understanding of the modern seawater U cycle). The differences between the observed trends and the expected ones show that the assumption of a constant offset between anoxic sediments and seawater might not be valid for the Precambrian, and great care should be exercised when applying knowledge of the modern U isotopic cycle to periods in Earth's history when the extent of anoxia was much greater than at the present.

uranium into the ocean F_{in}(μg/yr) is equal to the flux out F_{out}(μg/yr) given by the U burial rate B_i (μg U cm^{-2} yr^{-1}) integrated over the seafloor surface area A_i (cm^2) covered by a particular sink i,

$$F_{in} = F_{out} = \sum_i F_i = \sum_i \int_0^{A_i} B_i dA. \quad (7)$$

Splitting the sinks into anoxic (a), and non-anoxic (na), Eq. (7) becomes,

$$F_{in} = \int_0^{A_{na}} B_{na} dA + \int_0^{A_a} B_a dA. \quad (8)$$

The U burial rates in the past ocean are related to the modern (m subscript) burial rates in each sink by a dimensionless scaling factor ε,

$$B_{na} = \varepsilon_{na} B_{na,m}. \quad (9)$$

$$B_a = \varepsilon_a B_{a,m} \quad (10)$$

The U burial rates scale with U concentration in seawater at time t $[U]_{sw,t}$ following a power relationship (Reinhard et al., 2013),

$$\varepsilon_{na} = k_{na} [U]_{sw,t}^{\theta_{na}}. \quad (11)$$

$$\varepsilon_a = k_a [\mathrm{U}]_{sw,t}^{\theta_a}. \quad (12)$$

For the non-anoxic sink, we take k_{na} to be constant and we constrain it from the modern seawater U concentration $[U]_{sw,m}$ ($\varepsilon_{na,m} = 1$),

$$k_{na} = \frac{1}{[U]_{sw,m}^{\theta_{na}}}. \quad (13)$$

The modern burial rate for the non-anoxic sink is $B_{na,m} = F_{na,m}/A_{na,m}$, so that Eq. (9) becomes,

$$B_{na} = \left(\frac{[\mathrm{U}]_{sw,t}}{[\mathrm{U}]_{sw,m}}\right)^{\theta_{na}} \frac{F_{na,m}}{A_{na,m}}. \quad (14)$$

As discussed by Reinhard et al. (2013) and Sheen et al. (2018), one cannot assume that the anoxic sink scaling factor k_a remained constant as trace metal burial rate also depends on organic carbon burial rate (Algeo and Lyons, 2006). Modern anoxic burial rates are measured in shelf sediments, where organic burial rates are high due to high primary productivity. In the past, anoxia could have expanded into abyssal plains, which are characterized by lower carbon burial rates and presumably lower efficiency of redox metal removal (*e.g.,* U). In order to account for these two effects, we write k_a as a function of the organic carbon burial rate $B_{C_{org}}$ (mmol C cm^{-2} yr^{-1}),

$$k_a = \gamma B_{C_{org}}, \quad (15)$$

where γ is a parameter that did not change through time. The scaling factor relating anoxic U burial rate to seawater concentration therefore takes the following form (by combining Eqs. (12) and (15)),

$$\varepsilon_a = \gamma B_{C_{org}} [U]_{sw,t}^{\theta_a}. \quad (16)$$

The anoxic burial rate in Eq. (10) is therefore,

$$B_a = \gamma B_{C_{org}} [U]_{sw,t}^{\theta_a} B_{a,m}. \quad (17)$$

Integrating the burial rates over the surface area of the sinks, we have from Eq. (8),

$$F_{in} = \left(\frac{[\mathrm{U}]_{sw,t}}{[\mathrm{U}]_{sw,m}}\right)^{\theta_{na}} \frac{A_{na}}{A_{na,m}} F_{na,m} + \int_0^{A_a} \gamma [U]_{sw,t}^{\theta_a} B_{C_{org}} B_{a,m} dA. \quad (18)$$

Assuming that the oceans were homogeneous and given that $[U]_{sw,m}^{\theta_{na}}$, γ, $B_{na,m}$ and $B_{a,m}$ are constant in our model, we can rewrite Eq. (18) as,

$$F_{in} = \left(\frac{[\mathrm{U}]_{sw,t}}{[\mathrm{U}]_{sw,m}}\right)^{\theta_{na}} \frac{A_{na}}{A_{na,m}} F_{na,m} + \gamma [U]_{sw,t}^{\theta_a} B_{a,m} \times \int_0^{A_a} B_{C_{org}} dA. \quad (19)$$

We now focus on the anoxic flux (second term on the right side of Eq. (19)). The carbon burial rate per unit time per unit surface area depends on depth Z (m) following the equation (Middelburg et al., 1997; we assume that this relationship did not change through time),

$$B_{C_{org}} = \alpha 10^{-\beta Z}, \quad (20)$$

with $\alpha = 0.63$, $\beta = 0.00062$. Following Reinhard et al. (2013) and Sheen et al. (2018), we posit that anoxia expands from the continental shelf to abyssal plains. This is obviously a simplification as in the modern oceans, non-anoxic and anoxic environments coexist laterally at the same bathymetry. With this caveat in mind, we introduce $\zeta(A)$, a function that gives the seawater depth ζ above which seafloor covers a surface area A. The modern function $\zeta_m(A)$ is fitted using a linear function to bathymetric data from the Global Topography V19.1 database (Smith and Sandwell, 1997; Fig. 8),

$$\zeta_m(A) \simeq aA + b, \quad (21)$$

with $\zeta_m(A)$ in m and A in m^2, $a = 1.59 \times 10^{-15}$ and $b = 560$.

Equation (19) therefore takes the form,

$$F_{in} = \left(\frac{[\mathrm{U}]_{sw,t}}{[\mathrm{U}]_{sw,m}}\right)^{\theta_{na}} \frac{A_{na}}{A_{na,m}} F_{na,m} + \gamma [U]_{sw,t}^{\theta_a} B_{a,m} \times \int_0^{A_a} \alpha 10^{-\beta \zeta_m(A)} dA. \quad (22)$$

To constrain γ, we apply the expression for the anoxic sink to the modern ocean,

$$F_{a,m} = \gamma [U]_{sw,m}^{\theta_a} B_{a,m} \int_0^{A_{a,m}} \alpha 10^{-\beta \zeta_m(A)} dA, \quad (23)$$

from which we can express γ as,

$$\gamma = \frac{F_{a,m}}{[U]_{sw,m}^{\theta_a} B_{a,m} \int_0^{A_{a,m}} \alpha 10^{-\beta \zeta_m(A)} dA}. \quad (24)$$

We thus have for F_{in} (by combining Eqs. (22) and (24)),

$$F_{in} = \left(\frac{[\mathrm{U}]_{sw,t}}{[\mathrm{U}]_{sw,m}}\right)^{\theta_{na}} \frac{A_{na}}{A_{na,m}} F_{na,m} + \left(\frac{[\mathrm{U}]_{sw,t}}{[\mathrm{U}]_{sw,m}}\right)^{\theta_a} \times \frac{\int_0^{A_a} 10^{-\beta \zeta_m(A)} dA}{\int_0^{A_{a,m}} 10^{-\beta \zeta_m(A)} dA} F_{a,m}. \quad (25)$$

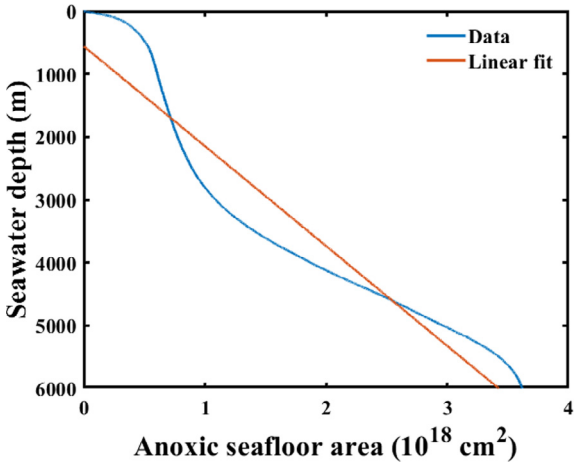

Fig. 8. Seawater depth *vs.* seafloor area above that depth (ζ_m function in the main text). The blue curve is the modern Global Topography V19.1 database (Smith and Sandwell 1997). The orange line is an approximate best fit line (Eq. (21)).

We are primarily interested in evaluating how the U residence time could have changed in the past. The residence time τ (kyr) depends on the U input and output fluxes (μg U/yr) and the U inventory of seawater as expressed in Eq. (6). Reinhard et al. (2013) showed that for Mo in modern anoxic basins, θ_a was apparently close to 0.25. In our calculation of residence time, we therefore explore θ_a values for U between 0.25 and 1.

4.3.1. Approach 1. Constant U input flux after the GOE

Reinhard et al. (2013) and Sheen et al. (2018) applied their mass-balance model to the Proterozoic Eon to constrain the extent of oceanic anoxia based on the concentrations of authigenic redox metals (Cr, Mo and Re) in shales. For that purpose, they assumed that once the GOE started, the riverine flux of redox-sensitive elements stayed the same and was equal to the modern value. The justification for this assumption is that after the GOE, the atmosphere became oxygenated and redox-sensitive minerals disappeared from detrital sediments, so if crustal weathering was the same as today, riverine delivery of redox-sensitive elements must have been similar to the present levels. As a first approach, we make the same assumption to calculate the residence time of U in the oceans after the GOE (as discussed below, we use other approaches before the GOE). If we keep the influx equal to the modern value $F_{in,m}$, we can use the relation in Eq. (25) and the inverse function $[U]_{sw,t} = \phi^{-1}(F_{in,m})$ to calculate the residence time as a function of anoxia extent,

$$\tau = \frac{M_{sw}\phi^{-1}(F_{in,m})}{F_{in,m}}. \tag{26}$$

In Fig. 9, we plot τ as a function of A_a. The residence time of U in seawater decreases significantly if the anoxic seafloor area exceeds ~ 4% of the total seafloor. Knowing the influx, we can calculate seawater concentration using Eq. (25) (Fig. S2), as well as the U concentrations in carbonates and black shales (Fig. S3, the details of the calculations are provided in Sections 4.3.2 and 4.3.3). Some model parameters would yield black shale and carbonate U concentrations that are clearly inconsistent with the rock record, and we highlight with thick solid lines in Fig. 9 the range of values of seafloor anoxia that yield realistic concentrations. As expected, the seawater U residence time decreases with a greater extent of anoxia and it could have reached ~18 kyr for $\theta_a = 0.75$ and around ≥30% anoxia. This value for the seawater U residence time is larger than the modern ocean mixing timescale of ~1 kyr but is much lower than the modern seawater U residence time of ~400 kyr.

4.3.2. Approach 2. Using authigenic U concentration in shale

The constant input flux assumption used in Section 4.3.1 (this study; Sheen et al., 2018; Reinhard et al., 2013) may be reasonable after the GOE. However, it is invalid before the GOE as detrital uraninite was able to survive weathering under the anoxic atmosphere that prevailed during that time. Below, we explore two approaches that relax the assumption of a constant input flux and use instead sedimentary data to constrain the seawater U residence time, starting with the shale data.

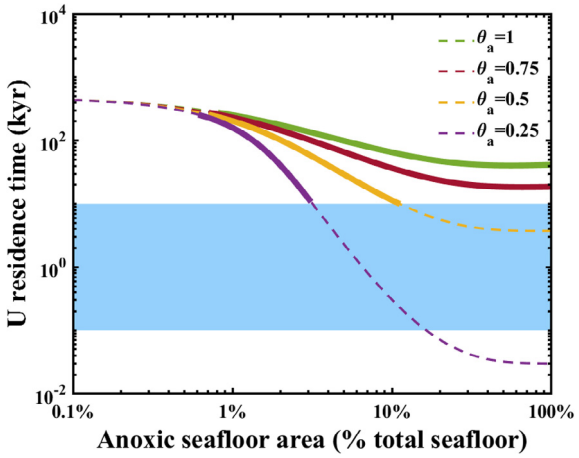

Fig. 9. Modeled U residence time with increasing seafloor anoxia based on the assumption of constant modern-like U riverine flux after the GOE (Reinhard et al., 2013) with different θ_a exponents. The blue box shows the probable ocean mixing timescale range in the Precambrian (0.1–10 kyr, see discussion in Section 4.4). The thick solid lines are those that yield realistic U concentrations in carbonates and shales (see Fig. S3).

In the framework of our model, we can relate the concentration of authigenic U in black shales $[U]_{bs}$ (ppm) to the concentration of U in seawater. Since shale samples are from continental margins, we integrate the anoxic burial rate B_a over the anoxic area A_a until it reaches the boundary of modern continental margins ($A_a \leq A_{CM} = 1.014 \times 10^{18}$ cm^2, 28% of global seafloor area, Carleton, 2000). The total amount of U deposited per unit time in anoxic sediments on the continental margin $F_{a,CM}$ is given by,

$$F_{a,CM} = \int_0^{min(A_a,A_{CM})} B_a dA = \left(\frac{[U]_{sw,t}}{[U]_{sw,m}}\right)^{\theta_a} \frac{\int_0^{min(A_a,A_{CM})} 10^{-\beta\zeta_m(A)} dA}{\int_0^{A_{a,m}} 10^{-\beta\zeta_m(A)} dA} F_{a,m}. \tag{27}$$

The black shale bulk mass accumulation rate R is calculated using the dry bulk density measured in the Cariaco Basin (0.606 g/cm^3 of dry solid per volume of wet sediment; Sheen et al., 2018, Peterson et al., 2000) multiplied by a sedimentation rate S of 5–100 m/Myr (Einsele, 1992). The average modern value is ~33 m/Myr (Partin et al., 2013a) and we explore the range 5–100 m/Myr to illustrate the sensitivity of the calculation to this parameter. These three sedimentation rates result in bulk mass accumulation rate values of 0.3×10^{-3}, 2.0×10^{-3} and 6.1×10^{-3} g cm^{-2} yr^{-1}, respectively. The predicted authigenic U concentration in anoxic shales $[U]_{bs}$ (ppm) is obtained by dividing Eq. (27) by the total sediment flux in shelf anoxic sediments $R \times \min(A_a, A_{CM})$,

$$[U]_{bs} = \frac{\int_0^{min(A_a,A_{CM})} B_a dA}{R \times min(A_a, A_{CM})} = \frac{1}{R \times min(A_a, A_{CM})} \left(\frac{[U]_{sw,t}}{[U]_{sw,m}}\right)^{\theta_a} \times \frac{\int_0^{min(A_a,A_{CM})} 10^{-\beta\zeta_m(A)} dA}{\int_0^{A_{a,m}} 10^{-\beta\zeta_m(A)} dA} F_{a,m}. \quad (28)$$

For a given extent of anoxia A_a, this equation establishes a relationship between the authigenic U enrichment in black shale $[U]_{bs}$ and the U concentration in seawater $[U]_{sw,t}$. We take authigenic U concentrations in black shales from Partin et al. (2013a) (Table 2) to solve Eq. (28) for the concentration of U in seawater as a function of the extent of anoxia,

$$[U]_{sw,t} = [U]_{sw,m} \left(\frac{[U]_{bs} \times R \times min(A_a, A_{CM})}{F_{a,m}} \frac{\int_0^{A_{a,m}} 10^{-\beta\zeta_m(A)} dA}{\int_0^{min(A_a,A_{CM})} 10^{-\beta\zeta_m(A)} dA} \right)^{1/\theta_a}. \quad (29)$$

Injecting Eqs. (29) to (25), we can calculate the U input flux at any geological time for a given extent of anoxia based on the available black shale record,

$$F_{in} = \left(\frac{[U]_{bs} \times R \times min(A_a, A_{CM})}{F_{a,m}} \frac{\int_0^{A_{a,m}} 10^{-\beta\zeta_m(A)} dA}{\int_0^{min(A_a,A_{CM})} 10^{-\beta\zeta_m(A)} dA} \right)^{\theta_{na}/\theta_a} \times \frac{A_{na}}{A_{na,m}} F_{na,m} + [U]_{bs} \times R \times min(A_a, A_{CM}) \frac{\int_0^{A_{a,m}} 10^{-\beta\zeta_m(A)} dA}{\int_0^{min(A_a,A_{CM})} 10^{-\beta\zeta_m(A)} dA}. \quad (30)$$

The residence time is the inventory in seawater divided by the input flux (Eq. (6)), which we can calculate by combining Eqs. (29) and (30),

$$\tau = \frac{M_{SW}[U]_{sw,m} \left(\frac{[U]_{bs} \times R \times min(A_a,A_{CM})}{F_{a,m}} \frac{\int_0^{A_{a,m}} 10^{-\beta\zeta_m(A)} dA}{\int_0^{min(A_a,A_{CM})} 10^{-\beta\zeta_m(A)} dA} \right)^{1/\theta_a}}{\left(\frac{[U]_{bs} \times R \times min(A_a,A_{CM})}{F_{a,m}} \frac{\int_0^{A_{a,m}} 10^{-\beta\zeta_m(A)} dA}{\int_0^{min(A_a,A_{CM})} 10^{-\beta\zeta_m(A)} dA} \right)^{\theta_{na}/\theta_a} \frac{A_{na}}{A_{na,m}} F_{na,m} + [U]_{bs} \times R \times min(A_a, A_{CM}) \frac{\int_0^{A_{a,m}} 10^{-\beta\zeta_m(A)} dA}{\int_0^{min(A_a,A_{CM})} 10^{-\beta\zeta_m(A)} dA}}. \quad (31)$$

Fig. 10 shows the U residence time calculated using black shale data as a function of the areal extent of anoxic sinks with different sedimentation rates in the Archean (left panel) and mid-Proterozoic (right panel). We also calculate and plot the predicted U concentration in carbonates using the approach described in Section 4.3.3 (Fig. S4) and the seawater concentration calculated using black shale data and Eq. (29) (Fig. S5). Some model parameters yield U concentrations in carbonates that are clearly inconsistent with the rock record (Fig. 1A). We also calculate and plot the predicted U input flux using Eq. (30) (Fig. S6), which adds another constraint to the possible residence time, as we can conservatively assume that the flux of dissolved U to the oceans was smaller in the Archean than what it is at present. We highlight with thick solid lines in Fig. 10 the range of values that yield realistic carbonate concentrations and input U flux. In the Archean and mid-Proterozoic, the residence time decreases with a greater extent of anoxia, and it could have reached ~18 kyr for $\theta_a = 0.75$,$S = 100$ m/Myr and around ≥20% anoxia in the Archean, and could have reached ~18 kyr for $\theta_a = 0.75$,$S = 33$ m/Myr and around ≥25% anoxia in the mid-Proterozoic, respectively. These modeled Precambrian seawater U residence times are much shorter than that of the modern ocean.

4.3.3. Approach 3. Using carbonate U concentration

A third approach for estimating the residence time of U in seawater when holding *flux in* constant is unjustified, is to

Table 2
Parameters used in U residence time modelling.

Parameter	Value	
Global seafloor area (cm^2)	3.62×10^{18}	
Mass of seawater (kg)	1.4×10^{21}	
Modern anoxic U burial rate (μg cm^{-2} yr^{-1})[a]	0.251	
Sedimentation rates (m/Myr)	33[a,b], 5[c],100[c]	
Modern anoxic sink area fraction (%)[d]	0.11	
Modern U seawater concentration (ppb)[a]	3.3	
Modern U riverine input flux (μg/yr)[b]	1×10^{16}	
	>2.4 Ga	1.9–0.8 Ga
Average $[U]_{bs}$ (ppm)[a]	1.14	2.96
$[U]_{sw,t}$ (ppb)[e]	0.10	0.14
*$[U]_{carb}$ (ppb)[e]	40	90
$[Ca]_{carb}$ (wt%)[e]	29.18	31.07
$[Ca]_{sw,t}$ (ppm)[f]	954	654

[a] Partin et al. (2013a).
[b] Dunk et al. (2002).
[c] Einsele (1992).
[d] Sheen et al. (2018).
[e] This study.
[f] Hardie (2003).
* We use here the 25th percentile $[U]_{carb}$ (ppb) of the measured values in the model calculation, which yields realistic $[U]_{sw}$ and U input flux while adopting the mean or median yields no satisfactory solution.

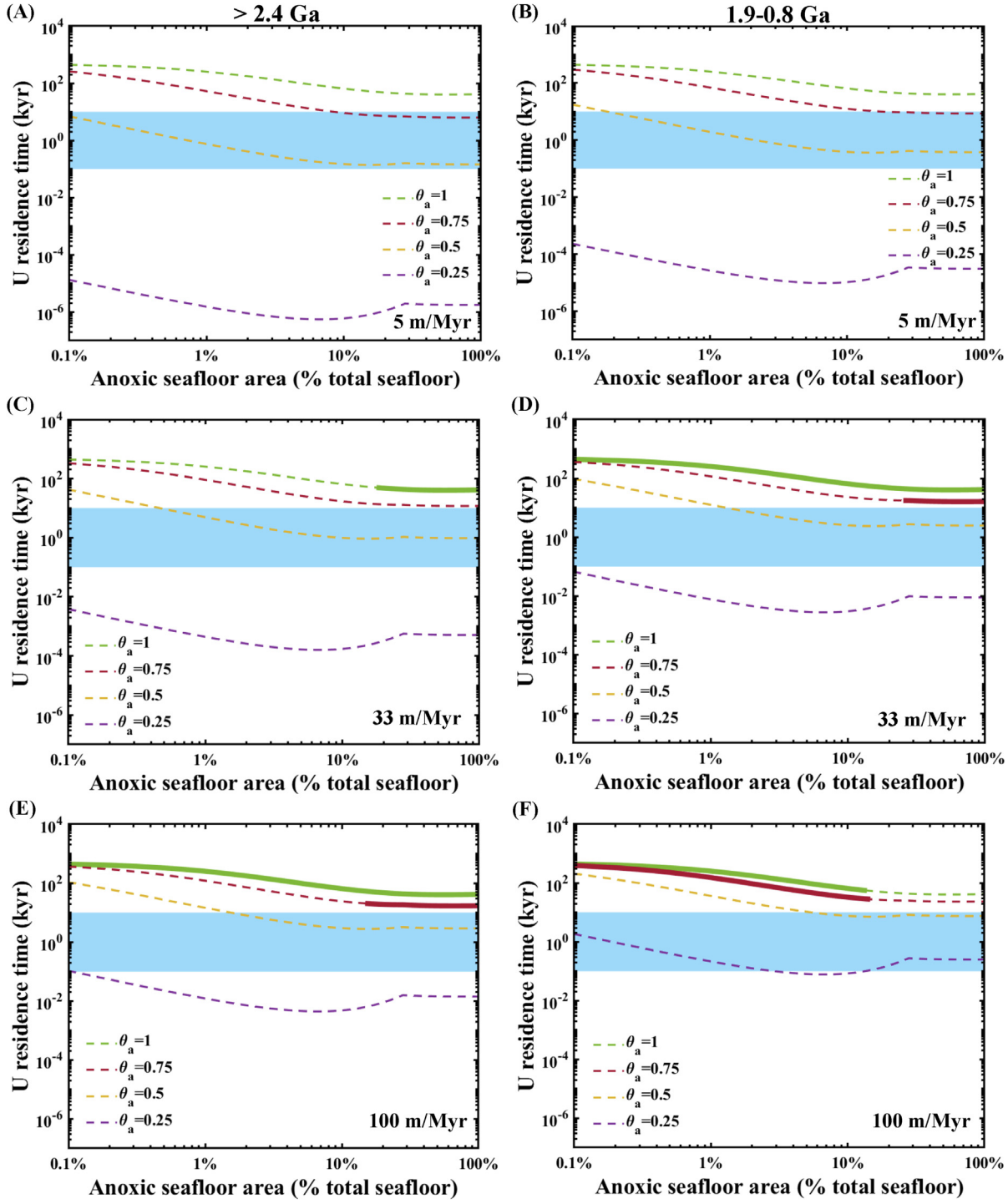

Fig. 10. Modeled U residence time with increasing seafloor anoxia using authigenic U enrichment in shales with different assumptions for the sedimentation rates (top panels S = 5, middle panels S = 33, and bottom panels S = 100 m/Myr) in the Archean (left) and mid-Proterozoic (right) (see text for details). The residence times calculated here relax the assumption of a constant influx of U to the oceans made in plotting Fig. 9. Different lines correspond to different exponents for the scaling of U burial rates with seawater concentration (Eqs. (12) and (17)). The blue box shows the probable ocean mixing timescale range in the Precambrian (0.1–10 kyr, see discussion in Section 4.4). The thick solid lines are those that yield realistic U concentrations in carbonates (Fig. S4) and U input flux (Fig. S6). We can conservatively say that the residence time decreases with a greater extent of anoxia, and in the Archean it could have reached ~18 kyr for $\theta_a = 0.75$,$S = 100$ m/Myr and around $\geq 20\%$ anoxia, and in the mid-Proterozoic it could have reached ~ 18 kyr for $\theta_a = 0.75$,$S = 33$ m/Myr and around $\geq 25\%$ anoxia.

use carbonates to infer seawater U concentration by using the U/Ca ratio,

$$[U]_{sw,t} = [Ca]_{sw,t} \times \frac{(U/Ca)_{carb,t}}{D_U}, \quad (32)$$

where D_U is the U/Ca distribution coefficient between carbonate and seawater, and $[Ca]_{sw,t}$ is the Ca concentration in seawater at time t (11 mmol/kg in modern seawater). For $(U/Ca)_{carb,t}$ (mass ratio), we use our carbonate measurements as well as the data compiled from the literature listed above (see Supplementary Table 1). The values of $[Ca]_{sw,t}$ and D_U relevant to the Precambrian are discussed below.

Based on analyses of primary fluid inclusions from marine halite, Brennan et al. (2004) estimated that $[Ca]_{sw}$ increased from 9.5–18.5 to 33.5–40 mmol/kg at the Neoproterozoic-Cambrian boundary between ~544 Ma and 515 Ma. Spear et al. (2014) also used the composition of primary fluid inclusions in marine halite to constrain the Ca concentration of ~830 Ma seawater to be between 9 and 12 mmol/kg. Blättler et al. (2018) provided a range of ~2.5–40 mmol/kg for $[Ca]_{sw}$ at ~2.1 Ga based on the study of a 2.1-billion-year-old marine evaporite succession from the Onega Parametric Hole (OPH), Karelia, Russia. These estimates are also consistent with the modeled secular variations in Precambrian seawater chemistry of Hardie (2003). Hardie (1996) modeled the secular $[Ca]_{sw}$ evolution during the Phanerozoic. We use the $[Ca]_{sw}$ value for each time interval from Hardie (1996, 2003) for calculation of $[U]_{sw,t}$.

The U/Ca distribution coefficient D_U is highly variable and has been estimated based on culture experiments (*e.g.*, Russell et al., 1994), co-precipitation experiments of inorganic aragonite and calcite (*e.g.*, Meece and Benninger, 1993; DeCarlo et al., 2015), studies of natural corals (*e.g.*, Swart and Hubbard, 1982; Gothmann et al., 2019), measurements of other biogenic carbonates (*e.g.*, Russell et al., 1994; Keul et al., 2013) and studies of coexisting porewater and carbonate in drill cores (Teichert et al., 2003; Maher et al., 2006). Although the average distribution coefficient through Earth's history might be expected to vary depending on proportion of aragonite precipitating from seawater, we find no clear correlation between the U concentration of carbonates and the inferred Mg/Ca ratio of coeval seawater (Halevy and Bachan, 2017; Hardie, 1996, 2003), suggesting minimal influence of primary carbonate mineralogy on U enrichment in the sedimentary carbonate record (see Fig. S7). We therefore assume a single value of 1.4 as calculated from measurements of uranium concentrations in calcite and pore water from the Ocean Drilling Program site 984 (Maher et al., 2006; Lau et al., 2016). This distribution coefficient might indeed be suitable for modeling U incorporation in Precambrian carbonates before the rise of calcifying organisms.

Equation (32) allows us to calculate the concentration of U in seawater from carbonate data, which we can then inject in Eq. (25) and Eq. (6) to calculate the U input flux and residence time,

$$F_{in} = \left(\frac{[Ca]_{sw,t} \times \frac{(U/Ca)_{carb,t}}{D_U}}{[U]_{sw,m}}\right)^{\theta_{na}} \frac{A_{na}}{A_{na,m}} F_{na,m} + \left(\frac{[Ca]_{sw,t} \times \frac{(U/Ca)_{carb,t}}{D_U}}{[U]_{sw,m}}\right)^{\theta_a} \times \frac{\int_0^{A_a} 10^{-\beta\zeta_m(A)} dA}{\int_0^{A_{a,m}} 10^{-\beta\zeta_m(A)} dA} F_{a,m}. \quad (33)$$

$$\tau = \frac{M_{sw}[Ca]_{sw,t} \times \frac{(U/Ca)_{carb,t}}{D_U}}{F_{in} = \left(\frac{[Ca]_{sw,t} \times \frac{(U/Ca)_{carb,t}}{D_U}}{[U]_{sw,m}}\right)^{\theta_{na}} \frac{A_{na}}{A_{na,m}} F_{na,m} + \left(\frac{[Ca]_{sw,t} \times \frac{(U/Ca)_{carb,t}}{D_U}}{[U]_{sw,m}}\right)^{\theta_a} \frac{\int_0^{A_a} 10^{-\beta\zeta_m(A)} dA}{\int_0^{A_{a,m}} 10^{-\beta\zeta_m(A)} dA} F_{a,m}}. \quad (34)$$

In Fig. 11, we plot the U residence time as a function of the areal extent of anoxia in the Archean (left) and mid-Proterozoic (right) using estimated U concentrations in seawater (Table 2) calculated from the measured U concentration in carbonates. We also calculated the predicted black shale concentration in Fig. S8 using Eq. (28). Some model parameters yield U concentrations in black shales that are clearly inconsistent with the rock record (see Fig. 1B). Some parameters also yield input dissolved U fluxes into the oceans that exceed the modern value, which is unrealistic (Fig. S9). We highlight with thick solid lines in Fig. 11 the range of values that yield realistic shale U concentrations and U input flux. The residence time decreases with a greater extent of anoxia and it could have reached ~18 kyr for $\theta_a = 0.75$ and around ≥30% anoxia in the Archean and mid-Proterozoic. Again, these modeled Precambrian seawater U residence times are much shorter than that of the modern ocean and are consistent with the modeled results in approach 1 and 2.

4.4. Mixing time in Archean and Proterozoic oceans

The above estimates indicate that the residence time of U may have been short, and in some cases approached the present-day seawater mixing timescale. However, the ancient ocean mixing timescale could have also differed significantly from that of today, as the oceans were likely characterized by different bathymetry, atmospheric forcing and tides. Highlighting the role of sea ice in Antarctic bottom-water formation, Lowe (1994) speculated that deep-ocean mixing timescale during the Archean may have been hundreds of thousands, or even millions of years, if the climate was warm enough for the Earth to be ice free. However, our current understanding of the deep-ocean circulation suggests that, while the location of bottom-water formation may change, the deep-ocean overturning circulation could remain active even with ice-free climates (*e.g.*, Enderton and Marshall, 2009; Jansen, 2017). Moreover, turbulent mixing processes ventilate the abyssal ocean even in the absence of a large-scale overturning circulation (*e.g.*, Burke et al., 2015).

To estimate whether the ocean mixing timescale would have differed substantially from the modern value during the Late Archean and Early Proterozoic, it is useful to consider the energy sources for ocean dynamics. The deep-ocean circulation and mixing processes derive their energy primarily from winds and tides (*e.g.*, Wunsch and Ferrari, 2004). Winds affect the circulation both directly by driving

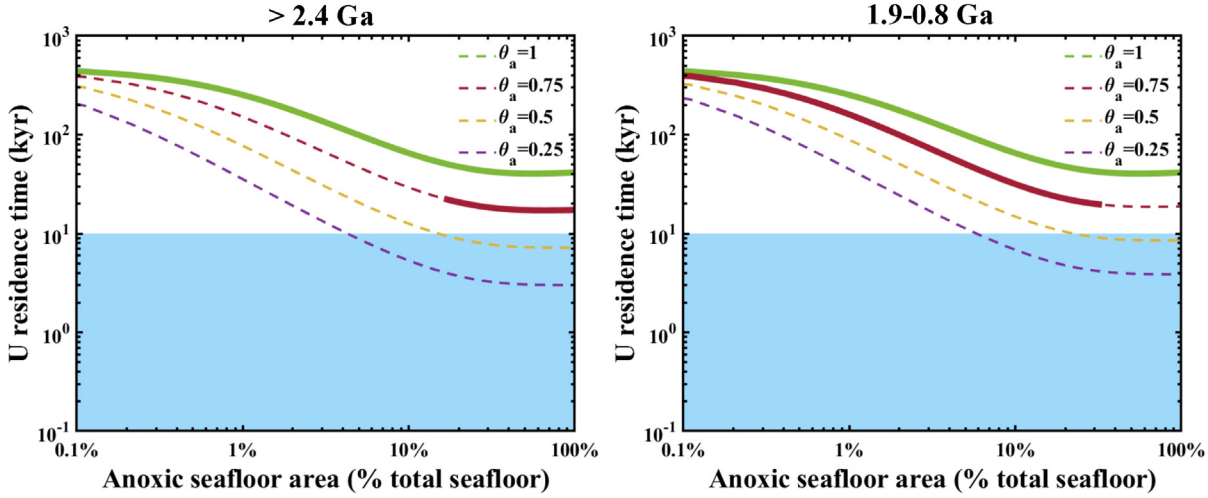

Fig. 11. Modeled U residence time with increasing seafloor anoxia using U in carbonates in the Archean (left) and mid-Proterozoic (right) (see text for details). Different lines correspond to different θ_a exponents. The residence times calculated here relax the assumption of a constant influx of U to the oceans made in plotting Fig. 9. The blue box shows the probable ocean mixing timescale range in the Precambrian (0.1–10 kyr, see discussion in Section 4.4). The thick solid lines correspond to parameters that yield realistic U concentrations in black shales (Fig. S8) and U input flux (Fig. S9). As shown, the residence time decreases with a greater extent of anoxia and it could have reached ~18 kyr for $\theta_a = 0.75$ and around $\geq$ 30% anoxia in the Archean and mid-Proterozoic.

divergent currents that pull waters from the deep ocean to the surface (*e.g.*, Nikurashin and Vallis, 2012) and indirectly via the generation of ocean turbulence. Tides also lead to the generation of small-scale turbulence in the ocean's interior and are likely to be the dominant source of energy for diapycnal mixing (*i.e.*, mixing across density surfaces), which in turn is fundamental to the maintenance of the deep-ocean overturning circulation and stratification (Wunsch and Ferrari, 2004).

Winds in the Archean may have differed from those today due to possible differences in the global mean temperature, Earth's rotation rate, continental area and configuration and/or atmospheric pressure. The climate of the Archean is poorly constrained, such that a wide range of global mean temperatures is possible based on empirical constraints (*e.g.*, Feulner, 2012). Modeling by O'Gorman and Schneider (2008) suggests that atmospheric eddy kinetic energy varies non-monotonically by about a factor of two across a wide range of climate states with global mean temperatures between −10 and +45 °C, with the highest energy obtained at a temperature similar to that of the present day. The planetary rotation rate in the Archean was likely faster, perhaps by about a factor of two (*e.g.* Webb, 1982). While Jenkins et al. (1993) found that this could have led to a significant reduction in mean tropospheric winds, Olson et al. (2020) showed that the surface wind stress, which governs the energy input into the oceans, was not very sensitive to rotation rate, with a halving of the day length leading to about a 15% decrease in the surface wind stress over the ocean. Surface pressure during the Archean remains uncertain, but most data point towards a lower surface pressure, perhaps around half of the present-day value (Catling and Zahnle, 2020). Olson et al. (2020) find that a halving of surface pressure leads to a reduction in surface wind stress of about 25%. Assuming that ocean surface currents are themselves proportional to the wind stress magnitude (as expected for the major ocean gyres – *e.g.,* Vallis, 2006) the energy input is proportional to the square of the wind stress, such that a 25% reduction in wind stress would amount to about a 45% decrease in wind-driven energy input. We conclude that the wind energy input to the Archean and Early Proterozoic oceans was probably somewhat lower than today, but within the same order of magnitude.

Tides during the Archean were affected by two compensating effects: the closer proximity of the moon would result in stronger tides, but the shorter day-length would lead to reduced tidal dissipation as oceanic normal modes become less efficiently excited by the tidal forcing (Webb, 1982; Bills and Ray, 1999). Modeling by Webb (1982) suggests that the average tidal energy dissipation in the ocean ~2 Ga was roughly similar to that today, while it may have been about twice as large at ~3 Ga. However, estimates of Archean tides remain highly uncertain, and the models at best provide only a rough estimate of the *average* tidal dissipation rates. Tidal resonances, which modulate energy dissipation, are affected by ocean basin geometry, adding further uncertainty to tidal dissipation in the Archean (*e.g.*, Bills and Ray, 1999).

A number of additional factors that are difficult to constrain can affect how efficiently the energy input of winds and tides is converted into motion that contributes to deep-ocean mixing. These factors include the continental configuration, which shapes deep-ocean overturning circulation (*e.g.*, Enderton and Marshall, 2009), as well as various parameters that influence the relationship between tidal energy dissipation and diapycnal mixing rates (such as seafloor topography and ocean stratification; *e.g.* Garrett and Kunze, 2007; Mashayek et al., 2017). Substantial uncertainties therefore remain with regards to the ocean mixing

timescale during the Late Archean and Early Proterozoic, but we do not expect a systematic difference beyond an order-of-magnitude from the present ocean mixing timescale, so a range of 0.1–10 kyr appears reasonable for much of Earth's history.

When Earth was dominated by anoxic bottom water, our calculations (Figs. 10 and 11) show that the residence time of U would have been much lower than present, possibly reaching ~18 kyr. It is thus conceivable that the deep-ocean mixing timescale and residence time of U in the Archean oceans may have been of similar order. Consequently, the isotopic composition of U in carbonates and shales may not necessarily reflect the global redox state of the oceans, but instead may only provide information about the regional redox conditions under which the carbonates and shales were deposited. In particular, we cannot exclude a substantial gradient in U concentration and isotopic composition between the upper layer of the oceans (where carbonates are deposited) and the deep-waters overlying anoxic sediments. It is even possible that ocean mixing itself governed the residence time of U in the oceans by limiting its supply to the sediments. This scenario offers a possible explanation for the observed similarity in $\delta^{238}U$ values of Archean carbonates and shales. Carbonates would have precipitated from surface waters whose U isotopic composition resembled the riverine source, while shales would have formed in deep waters where quantitative U removal under anoxic conditions would again record the U isotopic composition of the input flux, while leaving abyssal seawater depleted in ^{238}U (Fig. 12).

4.5. Non-uniformitarian U isotopic fractionation during deposition of Precambrian black shales

The mass balance of U isotopic composition of anoxic and other sinks assumes that our knowledge of the U cycle in the modern ocean is transferrable to deep times, as it uses empirical isotopic fractionation factors between sinks and seawater that are constrained based on analyses of recent sediments. Another conceivable explanation as to why Archean and Proterozoic carbonates have the same isotopic composition as continents is that the inferred U isotopic fractionation between U in anoxic sediments (black shales) and seawater constrained based on the modern ocean (Weyer et al., 2008; Montoya-Pino et al., 2010; Andersen et al., 2014; Holmden et al., 2015; Tissot and Dauphas, 2015; Andersen et al., 2016) is not applicable to the Archean world. In organic-rich sediments of the modern ocean, $\delta^{238}U$ values are shifted by ~+0.6‰ relative to U dissolved in seawater. If this fractionation factor was smaller in the Archean oceans, the removal of U with anoxic shales would not necessarily have induced a shift in the U isotopic composition of seawater and thus carbonates. If the isotopic fractionation during U uptake to carbonates was different than the modern, this would also affect our interpretations of the U sedimentary record. Uranium isotopic fractionation during removal to sediment can be affected by both equilibrium and kinetic processes, which are in turn affected by U speciation in seawater (Chen et al., 2016, 2017; Brown et al., 2018). We therefore start by calculating U speciation in ancient seawater (Fig. 13A). Chen et al. (2017) had calculated U speciation in the Phanerozoic and we extend that work to the Archean.

The geochemical modeling of aqueous U speciation follows Chen et al. (2017) and uses the PHREEQC program (Parkhurst and Appelo, 2013). The four most important aqueous U(VI) species (their total concentration accounts for >99% of U in solution) are $Ca_2UO_2(CO_3)_3(aq)$, $CaUO_2(CO_3)_3^{2-}$, $MgUO_2(CO_3)_3^{2-}$ and $UO_2(CO_3)_3^{4-}$. In Chen et al. (2017), $Ca_2UO_2(CO_3)_3(aq)$, $CaUO_2(CO_3)_3^{2-}$, and $MgUO_2(CO_3)_3^{2-}$ were added into the sit.dat database for the speciation calculation, with equilibrium constants from Dong and Brooks (2006). The species $Ca_2UO_2(CO_3)_3(aq)$ and $CaUO_2(CO_3)_3^{2-}$ are in the sit.dat database of the latest PHREEQC (version 3), so only $MgUO_2(CO_3)_3^{2-}$ and its equilibrium constant from Dong and Brooks (2006) were added to the sit.dat database in our simulation.

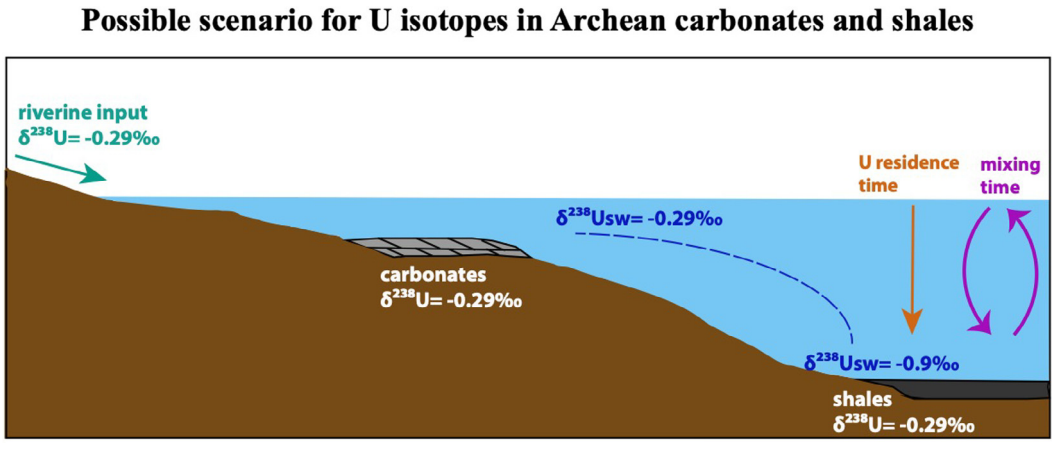

Fig. 12. Cartoon showing the possible scenario for the observed U isotopic composition in Precambrian carbonates and shales. Due to the similar magnitudes of the U residence time in ancient seawater and ocean mixing timescale, $\delta^{238}U$ values in carbonates and shales may not necessarily reflect the global redox state of the ocean, but instead only provide information about the provenance of U where the carbonates or shales were deposited (see detailed discussion in Section 4.4).

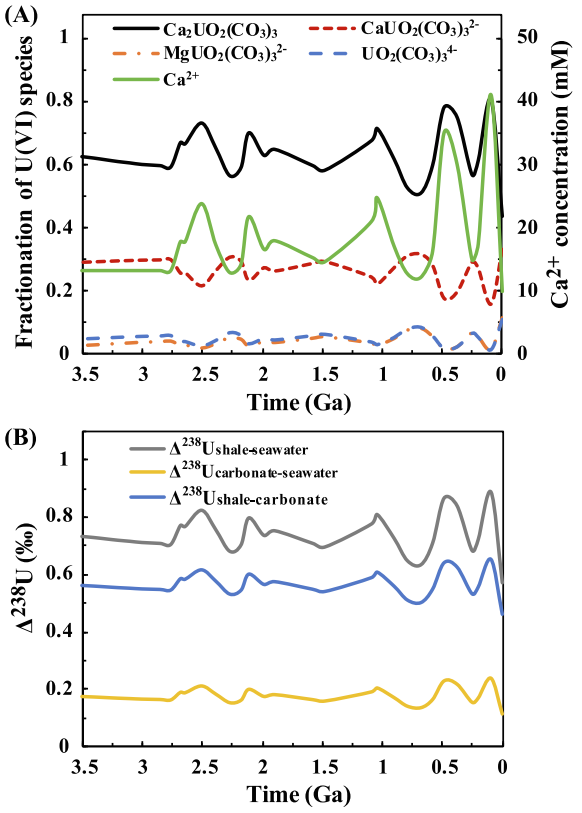

Fig. 13. U-speciation-induced secular variations of U isotopic fractionation factors. Panel (A) shows the U speciation through geologic time calculated using the PHREEQC program. Panel (B) shows the predicted influence of speciation on carbonate-seawater (Chen et al., 2016, 2017), shale-seawater (Brown et al., 2018), and carbonate-shale $\delta^{238}U$ fractionations using the calculated proportions of U species.

The major element seawater chemistry from the Archaean to the present is from Halevy and Bachan (2017) and Hardie (1996, 2003). Specifically, the simulation uses major ion concentrations (Cl^-, Na^+, K^+ and Mg^+) in seawater given by Halevy and Bachan (2017), as well as PCO_2, pH and Ca concentrations constrained by Hardie (1996, 2003). Uranium concentration in seawater is estimated in this study based on carbonate concentrations (see Section 4.3.2). Using these parameters, we find that the fraction of the neutral U(VI) species $Ca_2UO_2(CO_3)_3$(aq) in seawater is dominantly affected by Ca concentration in seawater. The dominant species are always $Ca_2UO_2(CO_3)_3$(aq) and $CaUO_2(CO_3)_3^{2-}$. The modern ocean comprises ~44% $Ca_2UO_2(CO_3)_3$ and ~33% $CaUO_2(CO_3)_3^{2-}$, while the ocean older than ~0.7 Ga would have comprised a larger fraction of neutral U species (~51% $Ca_2UO_2(CO_3)_3$ and ~32% $CaUO_2(CO_3)_3^{2-}$). Uranium aqueous speciation could have affected U isotopic fractionation in two manners: (1) During U(VI) removal to carbonates, U isotopic fractionation is affected by the U speciation in seawater as the equilibrium fractionation between $Ca_2UO_2(CO_3)_3$ and U in $CaCO_3$ is larger than the fractionation between $CaUO_2(CO_3)_3^{2-}$ and U in $CaCO_3$ (Chen et al., 2017). (2) During U removal to black shales, U is reduced from U(VI) to U(IV) and this can be affected by kinetic isotope effects that again are controlled by U speciation in seawater (Brown et al., 2018).

Based on our speciation calculation and the equilibrium isotopic fractionation factor given by Chen et al. (2017), we have calculated the equilibrium fractionation of U between U(VI) in carbonate and U(VI) in seawater and we find that in the Archean the isotopic fractionation could have been ~0.16–0.21‰ for $\delta^{238}U$ compared to ~0.1‰ at present (Fig. 13B). This is a small change and it is insufficient to explain the fact that carbonates have the same isotopic composition as black shales in the Archean and much of the Proterozoic.

Brown et al. (2018) studied experimentally the effect of reduction kinetics on U isotopic fractionation. They found that abiotic U reduction was associated with a larger isotopic fractionation when the dissolved species were dominated by neutrally charged aqueous Ca-U-CO_3 species. Conversely, the fractionation was smaller when the fraction of neutral dissolved species was low, and the reduction rate was high. Changes in U aqueous speciation through time could have affected the magnitude of U isotopic fractionation during U-reduction and removal to black shales. Brown et al. (2018) found a correlation between the fraction of the neutral species $Ca_2UO_2(CO_3)_3$(aq) and the isotope fractionation between reduced and oxidized U ($\Delta^{238}U_{IV\text{-}VI} = 0.854 \times fU_{neutral} + 0.2$). Using this relationship and our speciation calculation, we calculate the predicted isotopic fractionation between reduced U in sediments (black shales) and seawater (Fig. 13B). As shown in Fig. 13A, the larger fraction of neutral species in the Archean should have been associated with larger isotopic fractionation between black shales and seawater (carbonates) and this cannot explain the similar isotopic fractionation recorded by shales and carbonates from that Eon. This is also shown in Fig. 13B, where we plot the predicted fractionation between carbonate and shales, only considering changes in U speciation.

As discussed above, changes in the U speciation in seawater cannot explain our observation that both carbonates and black shales have $\delta^{238}U$ isotopic compositions similar to the crust during the Archean. Other processes may have been at play however, especially concerning U removal to black shales. Indeed, the pathway by which U(IV) is scavenged into reduced sediments is not fully resolved; it could involve both precipitation of uraninite in pore waters and adsorption onto organic matter and organic matter-coated clays (Anderson et al., 1989; Klinkhammer and Palmer, 1991; Cochran, 1992; Barnes and Cochran, 1993; Morford and Emerson, 1999; Bone et al., 2017). As discussed by Bone et al. (2017), the role of adsorption could be critical in aqueous systems with low U concentrations, as adsorption could lower the dissolved U(IV) concentration below the level required for uraninite precipitation. Based on studies of U concentrations in Precambrian BIFs (Partin et al., 2013b), shales (Partin et al., 2013a), and carbonates (this study; Gilleaudeau et al., 2019; Brüske et al., 2020a), it is likely that the U concentrations in the Archean and Proterozoic oceans were factors of 10–100 lower than they are in today's oceans. In this context, the

pathway for U removal into anoxic sediments could have been very different compared to the modern oceans, where both precipitation and adsorption are involved. It is thus conceivable that the U isotopic fractionation associated with U removal into anoxic sediments was different in the Archean and Proterozoic oceans compared to modern oceans where the ratio of dissolved uranium to organic carbon was presumably lower than in the modern oceans and the nature of organic matter was different (*i.e.*, mainly bacterial in origin; also comprising mature kerogen recycled from older sedimentary successions; Bekker and Holland, 2012). These suggestions are highly speculative and call for more field and experimental studies to better understand the controls on U removal and isotopic fractionation in shales. Interestingly, a recent study investigated the U isotopic composition of the modern and Silurian-Devonian shales, which were deposited in ferruginous settings and found that $\delta^{238}U$ values were highly variable with a muted fractionation factor on average (Cole et al., 2020). The authors also explored the effects on the mass balance model resulting from different reduction pathways with various apparent fractionation factors as well as different U mass accumulation rates. Their preferred interpretation is that the fractionation factors associated with ferruginous sinks are small (~0.1‰) and similar to the oxic sinks. If correct, $\delta^{238}U$ values may actually constrain the extent of euxinic sinks, which could be associated with larger fractionation factors (Gilleaudeau et al., 2019; Stockey et al., 2020). The anoxic but non-sulfidic conditions are thought to be extensive and dominant in the Precambrian oceans (cf. Planavsky et al., 2011; Poulton and Canfield, 2011) and if the results of Cole et al. (2020) are confirmed, their implication would support our interpretation that the U fractionation factor during reduction and burial in Precambrian black shales may have been different compared to that documented in modern euxinic ocean basins. A muted fractionation factor during U removal in Precambrian black shales would not shift the $\delta^{238}U$ value of seawater and carbonates away from the riverine source value, which could possibly explain our observations.

5. CONCLUSION

Uranium isotopic analyses of black shales and carbonates are increasingly used to reconstruct the extent of anoxia in critical periods of Earth's history. The applicability of this system relies on our understanding of the modern U cycle indicating that anoxic sediments tend to be enriched in the heavy isotopes of U relative to seawater by ~+0.6‰ in $\delta^{238}U$. If this U isotopic fractionation is applicable to the Precambrian sedimentary records, we should expect that once an oceanic U redox cycle was established, carbonates precipitated in the predominantly anoxic oceans would have their $\delta^{238}U$ values fractionated by −0.6‰ relative to the crustal value. We have measured the U isotopic compositions of 95 carbonates ranging in age from 3.25 to 0.63 Ga and our results reveal that on long timescale, the U isotopic composition of carbonates did not significantly evolve over the Precambrian and was always close to that of continental runoff. This suggests that some of the assumptions used to reconstruct ocean paleo-redox conditions from U isotope composition of carbonates and organic-rich shales may be invalid. In particular, we show that when oceanic anoxia increases significantly, the U residence time may decrease to a level comparable to the mixing timescale for the oceans. If correct, this implies that the common assumption that the U isotopic composition of Precambrian sediments reflects global ocean redox conditions might be flawed. Alternatively, the isotopic fractionation during U removal into Precambrian anoxic sediments could have been smaller than the modern value if the mechanism for U removal in shales was different. For example, anoxic and Fe-rich deep-ocean conditions, which have been inferred to be extensive in the early oceans, might have induced smaller fractionation to U uptake in these settings compared to the modern, anoxic and sulfidic, aerially restricted marine settings. If this interpretation is correct, it would imply a different operation of the U cycle, until the seawater sulfate reservoir dramatically increased in the late Neoproterozoic. More importantly, it would limit the use of the U isotope proxy to constrain Precambrian seawater redox state. Coupled carbonate and black shales studies in the same succession might help better constrain the underlying reason for muted U isotope fractionations in Precambrian carbonates and organic-rich shales.

AUTHOR CONTRIBUTIONS

Dauphas, Tissot, Chen, and Bekker conceived the project. Tissot, Bekker, Halverson, and Veizer made the sample selection. Chen performed the U isotopic analyses. Liu, Chen, and Dauphas modeled the influence of anoxia on U residence time. Nie modeled U speciation in seawater. Jansen evaluated the effects of the different forcing factors on the ocean mixing timescale in the Archean. Chen, Dauphas, and Jansen wrote the first draft of the manuscript, which was edited by all the co-authors.

Declaration of Competing Interest

The authors declare that they have no known competing financial interests or personal relationships that could have appeared to influence the work reported in this paper.

ACKNOWLEDGMENTS

This work was supported by NASA grants NNX17AE86G (LARS), NNX17AE87G and 80NSSC20K0821 (Emerging Worlds), and 80NSSC17K0744 (Habitable Worlds), and NSF grant EAR-2001098 (CSEDI) to ND; ACS Petroleum Research Fund grant 52964 to FT and ND; NSERC Discovery and Accelerator grants to AB; National Science Foundation (NSF OCE-1846821) to MFJ. Discussions with Andrew Heard, Clara Blättler and Jacob Waldbauer are greatly appreciated. We thank C. Stirling for her editorial handling of the manuscript and T.W. Dahl and two anonymous reviewers for their constructive comments that helped improve the quality of the manuscript.

APPENDIX A. SUPPLEMENTARY MATERIAL

Supplementary data to this article can be found online at https://doi.org/10.1016/j.gca.2021.01.040.

REFERENCES

Abe M., Suzuki T., Fujii Y., Hada M. and Hirao K. (2008) An ab initio molecular orbital study of the nuclear volume effects in uranium isotope fractionations. *J. Chem. Phys.* **129**, 164309.

Abshire M. L., Romaniello S. J., Kuzminov A. M., Cofrancesco J., Severmann S. and Riedinger N. (2020) Uranium isotopes as a proxy for primary depositional redox conditions in organic-rich marine systems. *Earth Planet. Sci. Lett.* **529**, 115878.

Algeo T. J. and Lyons T. W. (2006) Mo–total organic carbon covariation in modern anoxic marine environments: Implications for analysis of paleoredox and paleohydrographic conditions. *Paleoceanography* **21**.

Anbar A. D., Duan Y., Lyons T. W., Arnold G. L., Kendall B., Creaser R. A., Kaufman A. J., Gordon G. W., Scott C. and Garvin J. (2007) A whiff of oxygen before the great oxidation event? *Science (80-.)* **317**, 1903–1906.

Andersen M. B., Stirling C. H., Zimmermann B. and Halliday A. N. (2010) Precise determination of the open ocean 234U/238U composition. *Geochem. Geophys. Geosyst.* **11**.

Andersen M. B., Romaniello S., Vance D., Little S. H., Herdman R. and Lyons T. W. (2014) A modern framework for the interpretation of 238U/235U in studies of ancient ocean redox. *Earth Planet. Sci. Lett.* **400**, 184–194.

Andersen M. B., Vance D., Morford J. L., Bura-Nakić E., Breitenbach S. F. M. and Och L. (2016) Closing in on the marine 238U/235U budget. *Chem. Geol.* **420**, 11–22.

Andersen M. B., Stirling C. H. and Weyer S. (2017) Uranium isotope fractionation. *Rev. Mineral Geochem.* **82**, 799–850.

Andersen M. B., Matthews A., Vance D., Bar-Matthews M., Archer C. and de Souza G. F. (2018) A 10-fold decline in the deep Eastern Mediterranean thermohaline overturning circulation during the last interglacial period. *Earth Planet. Sci. Lett.* **503**, 58–67.

Anderson R. F., Fleisher M. Q. and LeHuray A. P. (1989) Concentration, oxidation state, and particulate flux of uranium in the Black Sea. *Geochim. Cosmochim. Acta* **53**, 2215–2224.

Asael D., Tissot F. L. H., Reinhard C. T., Rouxel O., Dauphas N., Lyons T. W., Ponzevera E., Liorzou C. and Chéron S. (2013) Coupled molybdenum, iron and uranium stable isotopes as oceanic paleoredox proxies during the Paleoproterozoic Shunga Event. *Chem. Geol.* **362**, 193–210.

Aspler L. B. and Chiarenzelli J. R. (2002) Mixed Siliciclastic-Carbonate Storm-Dominated Ramp in a Rejuvenated Palaeoproterozoic Intracratonic Basin: Upper Hurwitz Group, Nunavut, Canada. *Precambrian Sediment. Environ.: Mod. Approach Ancient Deposit. Syst.*, 293–321.

Azmy K., Kendall B., Brand U., Stouge S. and Gordon G. W. (2015) Redox conditions across the Cambrian-Ordovician boundary: Elemental and isotopic signatures retained in the GSSP carbonates. *Palaeogeogr. Palaeoclimatol. Palaeoecol.* **440**, 440–454.

Banner J. L. and Hanson G. N. (1990) Calculation of simultaneous isotopic and trace element variations during water-rock interaction with applications to carbonate diagenesis. *Geochim. Cosmochim. Acta* **54**, 3123–3137.

Barnes C. E. and Cochran J. K. (1993) Uranium geochemistry in estuarine sediments: controls on removal and release processes. *Geochim. Cosmochim. Acta* **57**, 555–569.

Bartlett R., Elrick M., Wheeley J. R., Polyak V., Desrochers A. and Asmerom Y. (2018) Abrupt global-ocean anoxia during the Late Ordovician–early Silurian detected using uranium isotopes of marine carbonates. *Proc. Natl. Acad. Sci.* **115**, 5896–5901.

Bartley J. K., Semikhatov M. A., Kaufman A. J., Knoll A. H., Pope M. C. and Jacobsen S. B. (2001) Global events across the Mesoproterozoic-Neoproterozoic boundary: C and Sr isotopic evidence from Siberia. *Precambrian Res.* **111**(1–4), 165–202.

Bekker A. and Eriksson K. A. (2003) Paleoproterozoic drowned carbonate platform on the southeastern margin of the Wyoming Craton: a record of the Kenorland breakup. *Precambrian Res.* **120**, 327–364.

Bekker A., Holland H. D., Wang P.-L., Rumble D., Stein H. J., Hannah J. L., Coetzee L. L. and Beukes N. J. (2004) Dating the rise of atmospheric oxygen. *Nature* **427**, 117–120.

Bekker A. and Holland H. D. (2012) Oxygen overshoot and recovery during the early Paleoproterozoic. *Earth Planet. Sci. Lett.* **317**, 295–304.

Bekker A., Sial A. N., Karhu J. A., Ferreira V. P., Noce C. M., Kaufman A. J. and Pimentel M. M. (2003) Chemostratigraphy of carbonates from the Minas Supergroup, Quadrilátero Ferryífero (Iron Quadrangle), Brazil: A stratigraphic record of early proterozoic atmospheric, biogeochemical and climactic change. *Am. J. Sci.* **303**(10), 865–904.

Bekker A., Karhu J. A., Eriksson K. A. and Kaufman A. J. (2003) Chemostratigraphy of Paleoproterozoic carbonate successions of the Wyoming Craton: tectonic forcing of biogeochemical change? *Precambrian Res.* **120**, 279–325.

Bekker A., Kaufman A. J., Karhu J. A. and Eriksson K. A. (2005) Evidence for Paleoproterozoic cap carbonates in North America. *Precambrian Res.* **137**, 167–206.

Bekker A., Karhu J. A. and Kaufman A. J. (2006) Carbon isotope record for the onset of the Lomagundi carbon isotope excursion in the Great Lakes area, North America. *Precambrian Res.* **148** (1–2), 145–180.

Bekker A., Holmden C., Beukes N. J., Kenig F., Eglinton B. and Patterson W. P. (2008) Fractionation between inorganic and organic carbon during the Lomagundi (2.22–2.1 Ga) carbon isotope excursion. *Earth Planet. Sci. Lett.* **271**(1–4), 278–291.

Bigeleisen J. (1996) Nuclear size and shape effects in chemical reactions. Isotope chemistry of the heavy elements. *J. Am. Chem. Soc.* **118**, 3676–3680.

Bills B. G. and Ray R. D. (1999) Lunar orbital evolution: A synthesis of recent results. *Geophys. Res. Lett.* **26**, 3045–3048.

Blättler C. L., Claire M. W., Prave A. R., Kirsimäe K., Higgins J. A., Medvedev P. V., Romashkin A. E., Rychanchik D. V., Zerkle A. L. and Paiste K. (2018) Two-billion-year-old evaporites capture Earth's great oxidation. *Science (80-.)* **360**, 320–323.

Bone S. E., Dynes J. J., Cliff J. and Bargar J. R. (2017) Uranium (IV) adsorption by natural organic matter in anoxic sediments. *Proc. Natl. Acad. Sci.* **114**, 711–716.

Bourdon B., Turner S., Henderson G. M. and Lundstrom C. C. (2003) Introduction to U-series geochemistry. *Rev. Mineral. Geochem.* **52**, 1–21.

Brennan S. T., Lowenstein T. K. and Horita J. (2004) Seawater chemistry and the advent of biocalcification. *Geology* **32**, 473–476.

Brennecka G. A., Herrmann A. D., Algeo T. J. and Anbar A. D. (2011) Rapid expansion of oceanic anoxia immediately before the end-Permian mass extinction. *Proc. Natl. Acad. Sci.* **108**, 17631–17634.

Brown S. T., Basu A., Ding X., Christensen J. N. and DePaolo D. J. (2018) Uranium isotope fractionation by abiotic reductive precipitation. *Proc. Natl. Acad. Sci.* **115**, 8688–8693.

Brüske A., Martin A. N., Rammensee P., Eroglu S., Lazarov M., Albut G., Schuth S., Aulbach S., Schoenberg R. and Beukes N. (2020a) The onset of oxidative weathering traced by uranium isotopes. *Precambrian Res.* **338**, 105583.

Brüske A., Weyer S., Zhao M.-Y., Planavsky N. J., Wegwerth A., Neubert N., Dellwig O., Lau K. V. and Lyons T. W. (2020b) Correlated molybdenum and uranium isotope signatures in modern anoxic sediments: Implications for their use as paleoredox proxy. *Geochim. Cosmochim. Acta* **270**, 449–474.

Bura-Nakić E., Andersen M. B., Archer C., de Souza G. F., Marguš M. and Vance D. (2018) Coupled Mo-U abundances and isotopes in a small marine euxinic basin: constraints on processes in euxinic basins. *Geochim. Cosmochim. Acta* **222**, 212–229.

Bura-Nakić E., Sondi I., Mikac N. and Andersen M. B. (2020) Investigating the molybdenum and uranium redox proxies in a modern shallow anoxic carbonate rich marine sediment setting of the Malo Jezero (Mljet Lakes, Adriatic Sea). *Chem. Geol.* **533**, 119441.

Burke A., Stewart A. L., Adkins J. F., Ferrari R., Jansen M. F. and Thompson A. F. (2015) The glacial mid-depth radiocarbon bulge and its implications for the overturning circulation. *Paleoceanography* **30**, 1021–1039.

Cao M., Daines S. J., Lenton T. M., Cui H., Algeo T. J., Dahl T. W., Shi W., Chen Z.-Q., Anbar A. and Zhou Y.-Q. (2020) Comparison of Ediacaran platform and slope δ238U records in South China: Implications for global-ocean oxygenation and the origin of the Shuram Excursion. *Geochim. Cosmochim. Acta* **287**, 111–124.

Carleton P. J. C. C. (2000) *Continental Shelf Limits: The Scientific and Legal Interface*. Oxford University Press on Demand.

Catling D. C. and Zahnle K. J. (2020) The Archean atmosphere. *Sci. Adv.* **6**, eaax1420.

Chen J. H., Edwards R. L. and Wasserburg G. J. (1986) 238U, 234U and232Th in seawater. *Earth Planet. Sci. Lett.* **80**, 241–251.

Chen X., Romaniello S. J., Herrmann A. D., Wasylenki L. E. and Anbar A. D. (2016) Uranium isotope fractionation during coprecipitation with aragonite and calcite. *Geochim. Cosmochim. Acta* **188**, 189–207.

Chen X., Romaniello S. J. and Anbar A. D. (2017) Uranium isotope fractionation induced by aqueous speciation: Implications for U isotopes in marine CaCO3 as a paleoredox proxy. *Geochim. Cosmochim. Acta* **215**, 162–172.

Chen X., Romaniello S. J., Herrmann A. D., Hardisty D., Gill B. C. and Anbar A. D. (2018a) Diagenetic effects on uranium isotope fractionation in carbonate sediments from the Bahamas. *Geochim. Cosmochim. Acta* **237**, 294–311.

Chen X., Romaniello S. J., Herrmann A. D., Samankassou E. and Anbar A. D. (2018b) Biological effects on uranium isotope fractionation (238U/235U) in primary biogenic carbonates. *Geochim. Cosmochim. Acta* **240**, 1–10.

Cheng H., Edwards R. L., Shen C.-C., Polyak V. J., Asmerom Y., Woodhead J., Hellstrom J., Wang Y., Kong X. and Spötl C. (2013) Improvements in 230Th dating, 230Th and 234U half-life values, and U-Th isotopic measurements by multi-collector inductively coupled plasma mass spectrometry. *Earth Planet. Sci. Lett.* **371**, 82–91.

Cheng K., Elrick M. and Romaniello S. J. (2020) Early Mississippian ocean anoxia triggered organic carbon burial and late Paleozoic cooling: Evidence from uranium isotopes recorded in marine limestone. *Geology* **48**, 363–367.

Clarkson M. O., Stirling C. H., Jenkyns H. C., Dickson A. J., Porcelli D., Moy C. M., von Strandmann P. A. E. P., Cooke I. R. and Lenton T. M. (2018) Uranium isotope evidence for two episodes of deoxygenation during Oceanic Anoxic Event 2. *Proc. Natl. Acad. Sci.* **115**, 2918–2923.

Clarkson M. O., Müsing K., Andersen M. B. and Vance D. (2020) Examining pelagic carbonate-rich sediments as an archive for authigenic uranium and molybdenum isotopes using reductive cleaning and leaching experiments. *Chem. Geol.* **539**, 119412.

Cochran, J.K., 1992. The oceanic chemistry of the uranium-and thorium-series nuclides. In: Uranium-series Disequilibrium: Applications to Earth, Marine, and Environmental Sciences. second ed.

Cole D. B., Planavsky N. J., Longley M., Böning P., Wilkes D., Wang X., Swanner E. D., Wittkop C., Loydell D. and Busigny V. (2020) Uranium isotope fractionation in non-sulfidic anoxic settings and the global uranium isotope mass balance. *Global Biogeochem. Cycles*, e2020GB006649.

Dahl T. W., Boyle R. A., Canfield D. E., Connelly J. N., Gill B. C., Lenton T. M. and Bizzarro M. (2014) Uranium isotopes distinguish two geochemically distinct stages during the later Cambrian SPICE event. *Earth Planet. Sci. Lett.* **401**, 313–326.

Dahl T. W., Connelly J. N., Kouchinsky A., Gill B. C., Månsson S. F. and Bizzarro M. (2017) Reorganisation of Earth's biogeochemical cycles briefly oxygenated the oceans 520 Myr ago. *Geochem. Perspect. Lett.* **3**(2), 210–220.

Dahl T. W., Connelly J. N., Li D., Kouchinsky A., Gill B. C., Porter S., Maloof A. C. and Bizzarro M. (2019) Atmosphere–ocean oxygen and productivity dynamics during early animal radiations. *Proc. Natl. Acad. Sci.* **116**, 19352–19361.

DeCarlo T. M., Gaetani G. A., Holcomb M. and Cohen A. L. (2015) Experimental determination of factors controlling U/Ca of aragonite precipitated from seawater: Implications for interpreting coral skeleton. *Geochim. Cosmochim. Acta* **162**, 151–165.

del Rey Á., Havsteen J. C., Bizzarro M. and Dahl T. W. (2020) Untangling the diagenetic history of uranium isotopes in marine carbonates: a case study tracing the δ238U composition of late Silurian oceans using calcitic brachiopod shells. *Geochim. Cosmochim. Acta* **287**, 93–110.

DePaolo D. J., Maher K. and Christensen J. N. (2003) Measuring the timescales of sediment production, transport, and deposition-U-234 sediment comminution ages. *AGUFM* **2003**, V11H–V107.

Dong W. and Brooks S. C. (2006) Determination of the formation constants of ternary complexes of uranyl and carbonate with alkaline earth metals (Mg2+, Ca2+, Sr2+, and Ba2+) using anion exchange method. *Environ. Sci. Technol.* **40**, 4689–4695.

Dunk R. M., Mills R. A. and Jenkins W. J. (2002) A reevaluation of the oceanic uranium budget for the Holocene. *Chem. Geol.* **190**, 45–67.

Einsele G. (1992) *Sedimentary Basins: Evolution, Facies, and Sedimentary Budget*. Springer-Verlag.

Elrick M., Polyak V., Algeo T. J., Romaniello S., Asmerom Y., Herrmann A. D., Anbar A. D., Zhao L. and Chen Z.-Q. (2017) Global-ocean redox variation during the middle-late Permian through Early Triassic based on uranium isotope and Th/U trends of marine carbonates. *Geology* **45**, 163–166.

Enderton D. and Marshall J. (2009) Explorations of atmosphere–ocean–ice climates on an aquaplanet and their meridional energy transports. *J. Atmos. Sci.* **66**, 1593–1611.

Endrizzi F. and Rao L. (2014) Chemical speciation of U (VI) in marine environments: Complexation of Ca2+ and Mg2+ with (UO2)(CO3) 3 4-and the effect on the extraction of uranium from seawater. *Chem. – Eur. J.* **20**(44), 14499–14506.

Fairchild I. J. and Hambrey M. J. (1995) Vendian basin evolution in East Greenland and NE Svalbard. *Precambrian Res.* **73**, 217–233.

Farquhar, J., Zerkle, A.L., Bekker, A., 2014. Geologic and geochemical constraints on Earth's early atmosphere. Treatise on Geochemisty. second ed. pp. 91–138.

Farquhar J., Zerkle A. L. and Bekker A. (2011) Geological constraints on the origin of oxygenic photosynthesis. *Photosynth. Res.* **107**, 11–36.

Feulner G. (2012) The faint young Sun problem. *Rev. Geophys.* **50** (2), RG2006.

Garrett C. and Kunze E. (2007) Internal tide generation in the deep ocean. *Annu. Rev. Fluid Mech.* **39**, 57–87.

Gilleaudeau G. J., Romaniello S. J., Luo G., Kaufman A. J., Zhang F., Klaebe R. M., Kah L. C., Azmy K., Bartley J. K. and Zheng W. (2019) Uranium isotope evidence for limited euxinia in mid-Proterozoic oceans. *Earth Planet. Sci. Lett.* **521**, 150–157.

Gothmann A. M., Higgins J. A., Adkins J. F., Broecker W., Farley K. A., McKeon R., Stolarski J., Planavsky N., Wang X. and Bender M. L. (2019) A Cenozoic record of seawater uranium in fossil corals. *Geochim. Cosmochim. Acta* **250**, 173–190.

Gumsley A. P., Chamberlain K. R., Bleeker W., Söderlund U., de Kock M. O., Larsson E. R. and Bekker A. (2017) Timing and tempo of the Great Oxidation Event. *Proc. Natl. Acad. Sci.* **114**, 1811–1816.

Halevy I. and Bachan A. (2017) The geologic history of seawater pH. *Science (80-.)* **355**, 1069–1071.

Halverson G. P., Kunzmann M., Strauss J. V. and Maloof A. C. (2018) The Tonian-Cryogenian transition in Svalbard. *Precambrian Res.* **319**, 79–95.

Hardie L. A. (1996) Secular variation in seawater chemistry: An explanation for the coupled secular variation in the mineralogies of marine limestones and potash evaporites over the past 600 my. *Geology* **24**, 279–283.

Hardie L. A. (2003) Secular variations in Precambrian seawater chemistry and the timing of Precambrian aragonite seas and calcite seas. *Geology* **31**, 785–788.

Hardisty D. S., Lu Z., Planavsky N. J., Bekker A., Philippot P., Zhou X. and Lyons T. W. (2014) An iodine record of Paleoproterozoic surface ocean oxygenation. *Geology* **42**, 619–622.

Hardisty D. S., Lu Z., Bekker A., Diamond C. W., Gill B. C., Jiang G., Kah L. C., Knoll A. H., Loyd S. J. and Osburn M. R. (2017) Perspectives on Proterozoic surface ocean redox from iodine contents in ancient and recent carbonate. *Earth Planet. Sci. Lett.* **463**, 159–170.

Henderson G. M., Slowey N. C. and Haddad G. A. (1999) Fluid flow through carbonate platforms: Constraints from 234U/238U and Cl− in Bahamas pore-waters. *Earth Planet. Sci. Lett.* **169**, 99–111.

Henderson G. M., Slowey N. C. and Fleisher M. Q. (2001) U-Th dating of carbonate platform and slope sediments. *Geochim. Cosmochim. Acta* **65**, 2757–2770.

Herrington P. M. and Fairchild I. J. (1989) Carbonate shelf and slope facies evolution prior to Vendian glaciation, central East Greenland. In *The Caledonide Geology of Scandinavia* (ed. R. A. Gayer). Graham Trotman, London, pp. 285–297.

Herrmann A. D., Gordon G. W. and Anbar A. D. (2018) Uranium isotope variations in a dolomitized Jurassic carbonate platform (Tithonian; Franconian Alb, Southern Germany). *Chem. Geol.* **497**, 41–53.

Hoffman P. F. and Halverson G. P. (2008) The Otavi Group of the Northern Platform and the Northern Margin Zone In: Miller, R.M (Ed.), In *The Geology of Namibia*, Vol. 2. Geological Survey of Namibia, Windhoek.

Holland H. D. (2002) Volcanic gases, black smokers, and the Great Oxidation Event. *Geochim. Cosmochim. Acta* **66**, 3811–3826.

Holland H. D. (2006) The oxygenation of the atmosphere and oceans. *Philos. Trans. R. Soc. B Biol. Sci.* **361**, 903–915.

Holland H. D. and Zimmermann H. (2000) The dolomite problem Revisited1. *Int. Geol. Rev.* **42**, 481–490.

Holmden C., Amini M. and Francois R. (2015) Uranium isotope fractionation in Saanich Inlet: A modern analog study of a paleoredox tracer. *Geochim. Cosmochim. Acta* **153**, 202–215.

Hood A. S., Planavsky N. J., Wallace M. W., Wang X., Bellefroid E. J., Gueguen B. and Cole D. B. (2016) Integrated geochemical-petrographic insights from component-selective δ238U of Cryogenian marine carbonates. *Geology* **44**, 935–938.

Jansen M. F. (2017) Glacial ocean circulation and stratification explained by reduced atmospheric temperature. *Proc. Natl. Acad. Sci.* **114**, 45–50.

Jenkins G. S., Marshall H. G. and Kuhn W. R. (1993) Precambrian climate: The effects of land area and Earth's rotation rate. *J. Geophys. Res. Atmos.* **98**, 8785–8791.

Johnston D. T., Poulton S. W., Goldberg T., Sergeev V. N., Podkovyrov V., Vorob'Eva N. G., Bekker A. and Knoll A. H. (2012) Late Ediacaran redox stability and metazoan evolution. *Earth Planet. Sci. Lett.* **335**, 25–35.

Jost A. B., Bachan A., van de Schootbrugge B., Lau K. V., Weaver K. L., Maher K. and Payne J. L. (2017) Uranium isotope evidence for an expansion of marine anoxia during the end-Triassic extinction. *Geochem. Geophys. Geosyst.* **18**, 3093–3108.

Kendall B., Brennecka G. A., Weyer S. and Anbar A. D. (2013) Uranium isotope fractionation suggests oxidative uranium mobilization at 2.50 Ga. *Chem. Geol.* **362**, 105–114.

Kendall B., Komiya T., Lyons T. W., Bates S. M., Gordon G. W., Romaniello S. J., Jiang G., Creaser R. A., Xiao S. and McFadden K. (2015) Uranium and molybdenum isotope evidence for an episode of widespread ocean oxygenation during the late Ediacaran Period. *Geochim. Cosmochim. Acta* **156**, 173–193.

Kendall B., Wang J., Zheng W., Romaniello S. J., Over D. J., Bennett Y., Xing L., Kunert A., Boyes C. and Liu J. (2020) Inverse correlation between the molybdenum and uranium isotope compositions of Upper Devonian black shales caused by changes in local depositional conditions rather than global ocean redox variations. *Geochim. Cosmochim. Acta* **287**, 141–164.

Keul N., Langer G., de Nooijer L. J., Nehrke G., Reichart G. and Bijma J. (2013) Incorporation of uranium in benthic foraminiferal calcite reflects seawater carbonate ion concentration. *Geochem. Geophys. Geosyst.* **14**, 102–111.

Khatiwala S., Primeau F. and Holzer M. (2012) Ventilation of the deep ocean constrained with tracer observations and implications for radiocarbon estimates of ideal mean age. *Earth Planet. Sci. Lett.* **325**, 116–125.

Klinkhammer G. P. and Palmer M. R. (1991) Uranium in the oceans: where it goes and why. *Geochim. Cosmochim. Acta* **55**, 1799–1806.

Korenaga J., Planavsky N. J. and Evans D. A. D. (2017) Global water cycle and the coevolution of the Earth's interior and surface environment. *Philos. Trans. R. Soc. A Math. Phys. Eng. Sci.* **375**, 20150393.

Ku T.-L., Knauss K. G. and Mathieu G. G. (1977) Uranium in open ocean: concentration and isotopic composition. *Deep Sea Res.* **24**, 1005–1017.

Kuznetsov A. B., Bekker A., Ovchinnikova G. V., Gorokhov I. M. and Vasilyeva I. M. (2017) Unradiogenic strontium and moderate-amplitude carbon isotope variations in early Tonian seawater after the assembly of Rodinia and before the Bitter Springs Excursion. *Precambrian Res.* **298**, 157–173.

Langmuir D. (1978) Uranium solution-mineral equilibria at low temperatures with applications to sedimentary ore deposits. *Geochim. Cosmochim. Acta* **42**, 547–569.

Lau K. V., Maher K., Altiner D., Kelley B. M., Kump L. R., Lehrmann D. J., Silva-Tamayo J. C., Weaver K. L., Yu M. and Payne J. L. (2016) Marine anoxia and delayed Earth system recovery after the end-Permian extinction. *Proc. Natl. Acad. Sci.* **113**, 2360–2365.

Lau K. V., Macdonald F. A., Maher K. and Payne J. L. (2017) Uranium isotope evidence for temporary ocean oxygenation in the aftermath of the Sturtian Snowball Earth. *Earth Planet. Sci. Lett.* **458**, 282–292.

Li Z., Cao M., Loyd S. J., Algeo T. J., Zhao H., Wang X., Zhao L. and Chen Z.-Q. (2020) Transient and stepwise ocean oxygena-

tion during the late Ediacaran Shuram Excursion: Insights from carbonate δ238U of northwestern Mexico. *Precambrian Res.*, 105741.

Livermore B. D., Dahl T. W., Bizzarro M. and Connelly J. N. (2020) Uranium isotope compositions of biogenic carbonates–Implications for U uptake in shells and the application of the paleo-ocean oxygenation proxy. *Geochim. Cosmochim. Acta* **287**, 50–64.

Lowe D. R. (1994) Early environments: constraints and opportunities for early evolution. *Early Life Earth*, 25–35.

Lu X., Kendall B., Stein H. J., Li C., Hannah J. L., Gordon G. W. and Ebbestad J. O. R. (2017) Marine redox conditions during deposition of Late Ordovician and Early Silurian organic-rich mudrocks in the Siljan ring district, central Sweden. *Chem. Geol.* **457**, 75–94.

Lyons T. W., Reinhard C. T. and Planavsky N. J. (2014) The rise of oxygen in Earth's early ocean and atmosphere. *Nature* **506**, 307–315.

Maher K., Steefel C. I., DePaolo D. J. and Viani B. E. (2006) The mineral dissolution rate conundrum: Insights from reactive transport modeling of U isotopes and pore fluid chemistry in marine sediments. *Geochim. Cosmochim. Acta* **70**, 337–363.

Maloubier M., Solari P. L., Moisy P., Monfort M., Den Auwer C. and Moulin C. (2015) XAS and TRLIF spectroscopy of uranium and neptunium in seawater. *Dalt. Trans.* **44**, 5417–5427.

Mänd K., Lalonde S. V., Robbins L. J., Thoby M., Paiste K., Kreitsmann T., Paiste P., Reinhard C. T., Romashkin A. E. and Planavsky N. J. (2020) Palaeoproterozoic oxygenated oceans following the Lomagundi-Jatuli Event. *Nat. Geosci.* **13**, 302–306.

Mashayek A., Salehipour H., Bouffard D., Caulfield C. P., Ferrari R., Nikurashin M., Peltier W. R. and Smyth W. D. (2017) Efficiency of turbulent mixing in the abyssal ocean circulation. *Geophys. Res. Lett.* **44**, 6296–6306.

Master S., Bekker A. and Hofmann A. (2010) A review of the stratigraphy and geological setting of the Palaeoproterozoic Magondi Supergroup, Zimbabwe-Type locality for the Lomagundi carbon isotope excursion. *Precambrian Res.* **182**(4), 254–273.

Meece D. E. and Benninger L. K. (1993) The coprecipitation of Pu and other radionuclides with CaCO3. *Geochim. Cosmochim. Acta* **57**, 1447–1458.

Middelburg J. J., Soetaert K. and Herman P. M. J. (1997) Empirical relationships for use in global diagenetic models. *Deep Sea Res. Part I Oceanogr. Res. Pap.* **44**, 327–344.

Mirota M. D. and Veizer J. (1994) Geochemistry of precambrian carbonates: VI. Aphebian albanel formations, Quebec, Canada. *Geochim. Cosmochim. Acta* **58**(7), 1735–1745.

Montoya-Pino C., Weyer S., Anbar A. D., Pross J., Oschmann W., van de Schootbrugge B. and Arz H. W. (2010) Global enhancement of ocean anoxia during Oceanic Anoxic Event 2: A quantitative approach using U isotopes. *Geology* **38**, 315–318.

Morford J. L. and Emerson S. (1999) The geochemistry of redox sensitive trace metals in sediments. *Geochim. Cosmochim. Acta* **63**, 1735–1750.

Nikurashin M. and Vallis G. (2012) A theory of the interhemispheric meridional overturning circulation and associated stratification. *J. Phys. Oceanogr.* **42**, 1652–1667.

Noordmann J., Weyer S., Montoya-Pino C., Dellwig O., Neubert N., Eckert S., Paetzel M. and Böttcher M. E. (2015) Uranium and molybdenum isotope systematics in modern euxinic basins: Case studies from the central Baltic Sea and the Kyllaren fjord (Norway). *Chem. Geol.* **396**, 182–195.

O'Gorman P. A. and Schneider T. (2008) Energy of midlatitude transient eddies in idealized simulations of changed climates. *J. Clim.* **21**, 5797–5806.

Olson S. L., Jansen M. and Abbot D. S. (2020) Oceanographic considerations for exoplanet life detection. *Astrophys. J.* **895**, 19.

Parkhurst D. L. and Appelo C. A. J. (2013) Description of input and examples for PHREEQC version 3: a computer program for speciation, batch-reaction, one-dimensional transport, and inverse geochemical calculations. *US Geol. Surv.*, No. 6-A43.

Partin C. A., Bekker A., Planavsky N. J., Scott C. T., Gill B. C., Li C., Podkovyrov V., Maslov A., Konhauser K. O. and Lalonde S. V. (2013a) Large-scale fluctuations in Precambrian atmospheric and oceanic oxygen levels from the record of U in shales. *Earth Planet. Sci. Lett.* **369**, 284–293.

Partin C. A., Lalonde S. V., Planavsky N. J., Bekker A., Rouxel O. J., Lyons T. W. and Konhauser K. O. (2013b) Uranium in iron formations and the rise of atmospheric oxygen. *Chem. Geol.* **362**, 82–90.

Peterson, L.C., Haug, G.H., Murray, R.W., Yarincik, K.M., King, J.W., Bralower, T.J., Kameo, K., Rutherford, S.D., Pearce, R. B., 2000. Late Quaternary stratigraphy and sedimentation at site 1002, Cariaco Basin (Venezuela). In: Proceedings of the Ocean Drilling Program, Scientific Results Ocean Drilling Program College Station, Texas, USA, pp. 85–99.

Phan T. T., Gardiner J. B., Capo R. C. and Stewart B. W. (2018) Geochemical and multi-isotopic (87Sr/86Sr, 143Nd/144Nd, 238U/235U) perspectives of sediment sources, depositional conditions, and diagenesis of the Marcellus Shale, Appalachian Basin, USA. *Geochim. Cosmochim. Acta* **222**, 187–211.

Planavsky N. J., McGoldrick P., Scott C. T., Li C., Reinhard C. T., Kelly A. E., Chu X., Bekker A., Love G. D. and Lyons T. W. (2011) Widespread iron-rich conditions in the mid-Proterozoic ocean. *Nature* **477**, 448–451.

Pope E. C., Bird D. K. and Rosing M. T. (2012) Isotope composition and volume of Earth's early oceans. *Proc. Natl. Acad. Sci.* **109**, 4371–4376.

Poulton S. W. and Canfield D. E. (2011) Ferruginous conditions: a dominant feature of the ocean through Earth's history. *Elements* **7**, 107–112.

Rainbird R. H., Davis W. J., Pehrsson S. J., Wodicka N., Rayner N. and Skulski T. (2010) Early Paleoproterozoic supracrustal assemblages of the Rae domain, Nunavut, Canada: Intracratonic basin development during supercontinent break-up and assembly. *Precambrian Res.* **181**(1–4), 167–186.

Ramdohr P. (1958) New observations of the ores of the Witwatersrand in South Africa and their genetic significance. *Geol. Soc. South Africa Trans.* **61**, 1–50.

Rasmussen B. and Buick R. (1999) Redox state of the Archean atmosphere: evidence from detrital heavy minerals in ca. 3250–2750 Ma sandstones from the Pilbara Craton, Australia. *Geology* **27**, 115–118.

Reinhard C. T., Planavsky N. J., Robbins L. J., Partin C. A., Gill B. C., Lalonde S. V., Bekker A., Konhauser K. O. and Lyons T. W. (2013) Proterozoic ocean redox and biogeochemical stasis. *Proc. Natl. Acad. Sci.* **110**, 5357–5362.

Romaniello S. J., Herrmann A. D. and Anbar A. D. (2013) Uranium concentrations and 238U/235U isotope ratios in modern carbonates from the Bahamas: Assessing a novel paleoredox proxy. *Chem. Geol.* **362**, 305–316.

Ross G. M., Villeneuve M. E. and Theriault R. J. (2001) Isotopic provenance of the lower Muskwa assemblage (Mesoproterozoic, Rocky Mountains, British Columbia): New clues to correlation and source areas. *Precambrian Res.* **111**(1–4), 57–77.

Rouxel O. J., Bekker A. and Edwards K. J. (2005) Iron isotope constraints on the Archean and Paleoproterozoic ocean redox state. *Science* **307**(5712), 1088–1091.

Russell A. D., Emerson S., Nelson B. K., Erez J. and Lea D. W. (1994) Uranium in foraminiferal calcite as a recorder of seawater uranium concentrations. *Geochim. Cosmochim. Acta* **58**, 671–681.

Sahoo S. K., Planavsky N. J., Kendall B., Wang X., Shi X., Scott C., Anbar A. D., Lyons T. W. and Jiang G. (2012) Ocean oxygenation in the wake of the Marinoan glaciation. *Nature* **489**, 546–549.

Schauble E. A. (2007) Role of nuclear volume in driving equilibrium stable isotope fractionation of mercury, thallium, and other very heavy elements. *Geochim. Cosmochim. Acta* **71**, 2170–2189.

Scott C., Lyons T. W., Bekker A., Shen Y., Poulton S. W., Chu X. and Anbar A. D. (2008) Tracing the stepwise oxygenation of the Proterozoic ocean. *Nature* **452**, 456–459.

Scott C., Wing B. A., Bekker A., Planavsky N. J., Medvedev P., Bates S. M., Yun M. and Lyons T. W. (2014) Pyrite multiple-sulfur isotope evidence for rapid expansion and contraction of the early Paleoproterozoic seawater sulfate reservoir. *Earth Planet. Sci. Lett.* **389**, 95–104.

Sheen A. I., Kendall B., Reinhard C. T., Creaser R. A., Lyons T. W., Bekker A., Poulton S. W. and Anbar A. D. (2018) A model for the oceanic mass balance of rhenium and implications for the extent of Proterozoic ocean anoxia. *Geochim. Cosmochim. Acta* **227**, 75–95.

Shields G. and Veizer J. (2002) Precambrian marine carbonate isotope database: Version 1.1. *Geochem. Geophys. Geosyst.* **3**, 1-of.

Siberlin C. and Wunsch C. (2011) Oceanic tracer and proxy time scales revisited. *Clim. Past* **7**(1), 27–39.

Smith W. H. F. and Sandwell D. T. (1997) Global sea floor topography from satellite altimetry and ship depth soundings. *Science (80-.)* **277**, 1956–1962.

Sønderholm M. and Tirsgaard H. (1993) Lithostratigraphic framework of the Upper Proterozoic Eleonore Bay Supergroup of East and North-East Greenland. *Grønlands Geolgiske Undersøgelsen* **167**, 3800.

Song H., Song H., Algeo T. J., Tong J., Romaniello S. J., Zhu Y., Chu D., Gong Y. and Anbar A. D. (2017) Uranium and carbon isotopes document global-ocean redox-productivity relationships linked to cooling during the Frasnian-Famennian mass extinction. *Geology* **45**, 887–890.

Spear N., Holland H. D., Garcia-Veígas J., Lowenstein T. K., Giegengack R. and Peters H. (2014) Analyses of fluid inclusions in Neoproterozoic marine halite provide oldest measurement of seawater chemistry. *Geology* **42**, 103–106.

Stirling C. H., Andersen M. B., Potter E.-K. and Halliday A. N. (2007) Low-temperature isotopic fractionation of uranium. *Earth Planet. Sci. Lett.* **264**, 208–225.

Stockey R. G., Cole D. B., Planavsky N. J., Loydell D. K., Frýda J. and Sperling E. A. (2020) Persistent global marine euxinia in the early Silurian. *Nat. Commun.* **11**, 1–10.

Swanner E. D., Planavsky N. J., Lalonde S. V., Robbins L. J., Bekker A., Rouxel O. J., Saito M. A., Kappler A., Mojzsis S. J. and Konhauser K. O. (2014) Cobalt and marine redox evolution. *Earth Planet. Sci. Lett.* **390**, 253–263.

Swart P. K. and Hubbard J. (1982) Uranium in scleractinian coral skeletons. *Coral Reefs* **1**, 13–19.

Taylor, S.R., McLennan, S.M., 1985. The Continental Crust: Its Composition and Evolution.

Teichert B. M. A., Eisenhauer A., Bohrmann G., Haase-Schramm A., Bock B. and Linke P. (2003) U/Th systematics and ages of authigenic carbonates from Hydrate Ridge, Cascadia Margin: recorders of fluid flow variations. *Geochim. Cosmochim. Acta* **67**, 3845–3857.

Telus M., Dauphas N., Moynier F., Tissot F. L. H., Teng F.-Z., Nabelek P. I., Craddock P. R. and Groat L. A. (2012) Iron, zinc, magnesium and uranium isotopic fractionation during continental crust differentiation: The tale from migmatites, granitoids, and pegmatites. *Geochim. Cosmochim. Acta* **97**, 247–265.

Teng F.-Z., Dauphas N. and Watkins J. M. (2017) Non-traditional stable isotopes: retrospective and prospective. *Rev. Mineral. Geochem.* **82**, 1–26.

Thomson D., Rainbird R. H., Planavsky N., Lyons T. W. and Bekker A. (2015) Chemostratigraphy of the Shaler Supergroup, Victoria Island, NW Canada: A record of ocean composition prior to the Cryogenian glaciations. *Precambrian Res.* **263**, 232–245.

Tissot F. L. H., Dauphas N. and Grove T. L. (2017) Distinct 238U/235U ratios and REE patterns in plutonic and volcanic angrites: Geochronologic implications and evidence for U isotope fractionation during magmatic processes. *Geochim. Cosmochim. Acta* **213**, 593–617.

Tissot F. L. H., Chen C., Go B. M., Naziemiec M., Healy G., Bekker A., Swart P. K. and Dauphas N. (2018) Controls of eustasy and diagenesis on the 238U/235U of carbonates and evolution of the seawater (234U/238U) during the last 1.4 Myr. *Geochim. Cosmochim. Acta* **242**, 233–265.

Tissot F. L. H. and Dauphas N. (2015) Uranium isotopic compositions of the crust and ocean: Age corrections, U budget and global extent of modern anoxia. *Geochim. Cosmochim. Acta* **167**, 113–143.

Tostevin R., Clarkson M. O., Gangl S., Shields G. A., Wood R. A., Bowyer F., Penny A. M. and Stirling C. H. (2019) Uranium isotope evidence for an expansion of anoxia in terminal Ediacaran oceans. *Earth Planet. Sci. Lett.* **506**, 104–112.

Turner E. C. and Bekker A. (2016) Thick sulfate evaporite accumulations marking a mid-Neoproterozoic oxygenation event (Ten Stone Formation, Northwest Territories, Canada). *GSA Bull.* **128**, 203–222.

Vallis G. K. (2006) *Atmospheric and Oceanic Fluid Dynamics: Fundamentals and Large-Scale Circulation*. Cambridge Univ..

Veizer J., Hoefs J., Ridler R. H., Jensen L. S. and Lowe D. R. (1989) Geochemistry of Precambrian carbonates: I. Archean hydrothermal systems. *Geochim. Cosmochim. Acta* **53**, 845–857.

Veizer J., Hoefs J., Lowe D. R. and Thurston P. C. (1989) Geochemistry of Precambrian carbonates: II. Archean greenstone belts and Archean sea water. *Geochim. Cosmochim. Acta.* **53**, 845–857.

Veizer J., Clayton R. N., Hlnton R. W., Von Brunn V., Mason T. R., Buck S. G. and Hoefs J. (1990) Geochemistry of Precambrian carbonates: 3-shelf seas and non-marine environments of the Archean. *Geochim. Cosmochim. Acta* **54**, 2717–2729.

Veizer J., Clayton R. N. and Hinton R. W. (1992) Geochemistry of Precambrian carbonates: IV. Early Paleoproterozoic (2.25 ±0.25 Ga) seawater. *Geochim. Cosmochim. Acta* **56**(3), 875–885.

Veizer J., Clayton R. N. and Hinton R. W. (1992a) Geochemistry of Precambrian carbonates: IV. Early Paleoproterozoic (2.25 ±0.25 Ga) seawater. *Geochim. Cosmochim. Acta* **56**, 875–885.

Veizer J., Plumb K. A., Clayton R. N., Hinton R. W. and Grotzinger J. P. (1992b) Geochemistry of Precambrian carbonates: V. late Paleoproterozoic seawater. *Geochim. Cosmochim. Acta* **56**, 2487–2501.

Verbruggen A., Alonso A., Eykens R., Kehoe F., Kuhn H., Richter S. and Aregbe Y. (2008) Preparation and certification of IRMM-3636, IRMM-3636a and IRMM-3636b. *JRC Sci. Tech Rep.*.

Wang X., Planavsky N. J., Reinhard C. T., Hein J. R. and Johnson T. M. (2016) A Cenozoic seawater redox record derived from 238U/235U in ferromanganese crusts. *Am. J. Sci.* **316**, 64–83.

Wang X., Planavsky N. J., Hofmann A., Saupe E. E., De Corte B. P., Philippot P., LaLonde S. V., Jemison N. E., Zou H. and Ossa F. O. (2018) A Mesoarchean shift in uranium isotope systematics. *Geochim. Cosmochim. Acta* **238**, 438–452.

Wang X., Ossa F. O., Hofmann A., Agangi A., Paprika D. and Planavsky N. J. (2020) Uranium isotope evidence for Mesoarchean biological oxygen production in shallow marine and continental settings. *Earth Planet. Sci. Lett.* **551**, 116583.

Webb D. J. (1982) Tides and the evolution of the Earth—Moon system. *Geophys. J. Int.* **70**, 261–271.

Wei G.-Y., Planavsky N. J., Tarhan L. G., Chen X., Wei W., Li D. and Ling H.-F. (2018) Marine redox fluctuation as a potential trigger for the Cambrian explosion. *Geology* **46**, 587–590.

Wei G.-Y., Planavsky N. J., Tarhan L. G., He T., Wang D., Shields G. A., Wei W. and Ling H.-F. (2020) Highly dynamic marine redox state through the Cambrian explosion highlighted by authigenic δ238U records. *Earth Planet. Sci. Lett.* **544**, 116361.

Weyer S., Anbar A. D., Gerdes A., Gordon G. W., Algeo T. J. and Boyle E. A. (2008) Natural fractionation of 238U/235U. *Geochim. Cosmochim. Acta* **72**, 345–359.

White D. A., Elrick M., Romaniello S. and Zhang F. (2018) Global seawater redox trends during the Late Devonian mass extinction detected using U isotopes of marine limestones. *Earth Planet. Sci. Lett.* **503**, 68–77.

Wörndle S., Crockford P. W., Kunzmann M., Bui T. H. and Halverson G. P. (2019) Linking the Bitter Springs carbon isotope anomaly and early Neoproterozoic oxygenation through I/[Ca+Mg] ratios. *Chem. Geol.* **524**, 119–135.

WunschC.andFerrariR.(2004)Verticalmixing,energy,andthegeneral circulationoftheoceans. *Annu. Rev. Fluid Mech.* **36**, 281–314.

Yang S., Kendall B., Lu X., Zhang F. and Zheng W. (2017) Uranium isotope compositions of mid-Proterozoic black shales: Evidence for an episode of increased ocean oxygenation at 1.36 Ga and evaluation of the effect of post-depositional hydrothermal fluid flow. *Precambrian Res.* **298**, 187–201.

Zhang F., Algeo T. J., Romaniello S. J., Cui Y., Zhao L., Chen Z.-Q. and Anbar A. D. (2018a) Congruent Permian-Triassic δ238U records at Panthalassic and Tethyan sites: Confirmation of global-oceanic anoxia and validation of the U-isotope paleoredox proxy. *Geology* **46**, 327–330.

Zhang F., Romaniello S. J., Algeo T. J., Lau K. V., Clapham M. E., Richoz S., Herrmann A. D., Smith H., Horacek M. and Anbar A. D. (2018b) Multiple episodes of extensive marine anoxia linked to global warming and continental weathering following the latest Permian mass extinction. *Sci. Adv.* **4**.

Zhang F., Xiao S., Kendall B., Romaniello S. J., Cui H., Meyer M., Gilleaudeau G. J., Kaufman A. J. and Anbar A. D. (2018c) Extensive marine anoxia during the terminal Ediacaran Period. *Sci. Adv.* **4**, eaan8983.

Zhang F., Algeo T. J., Cui Y., Shen J., Song H., Sano H., Rowe H. D. and Anbar A. D. (2019a) Global-ocean redox variations across the Smithian-Spathian boundary linked to concurrent climatic and biotic changes. *Earth-Sci. Rev.* **195**, 147–168.

Zhang F., Xiao S., Romaniello S. J., Hardisty D., Li C., Melezhik V., Pokrovsky B., Cheng M., Shi W. and Lenton T. M. (2019b) Global marine redox changes drove the rise and fall of the Ediacara biota. *Geobiology* **17**, 594–610.

Zhang F., Dahl T. W., Lenton T. M., Luo G., Shen S., Algeo T. J., Planavsky N., Liu J., Cui Y. and Qie W. (2020a) Extensive marine anoxia associated with the Late Devonian Hangenberg Crisis. *Earth Planet. Sci. Lett.* **533**, 115976.

Zhang F., Lenton T. M., del Rey Á., Romaniello S. J., Chen X., Planavsky N. J., Clarkson M. O., Dahl T. W., Lau K. V. and Wang W. (2020b) Uranium isotopes in marine carbonates as a global ocean paleoredox proxy: A critical review. *Geochim. Cosmochim. Acta* **287**, 27–49.

Zhang F., Shen S., Cui Y., Lenton T. M., Dahl T. W., Zhang H., Zheng Q., Wang W., Krainer K. and Anbar A. D. (2020c) Two distinct episodes of marine anoxia during the Permian-Triassic crisis evidenced by uranium isotopes in marine dolostones. *Geochim. Cosmochim. Acta* **287**, 165–179.

Zhao H., Algeo T. J., Liu Y., Chen Z.-Q., Zhang L., Hu Z. and Li Z. (2020) Lower Triassic carbonate δ238U record demonstrates expanded oceanic anoxia during Smithian Thermal Maximum and improved ventilation during Smithian-Spathian boundary cooling event. *Palaeogeogr. Palaeoclimatol. Palaeoecol.* **539**, 109393.

Associate editor: Claudine Stirling